Field observations of wave-averaged suspended sediment concentrations in the inner surf zone with varying storm conditions

van Wiechen, P.P.J.; de Vries, S.; Reniers, A.J.H.M.

DOI
10.1016/j.margeo.2024.107302

Publication date
2024

Document Version
Final published version

Published in
Marine Geology

Citation (APA)
van Wiechen, P. P. J., de Vries, S., & Reniers, A. J. H. M. (2024). Field observations of wave-averaged suspended sediment concentrations in the inner surf zone with varying storm conditions. *Marine Geology*, *473*, Article 107302. https://doi.org/10.1016/j.margeo.2024.107302

Marine Geology 473 (2024) 107302

Contents lists available at ScienceDirect

Marine Geology

journal homepage: www.elsevier.com/locate/margo

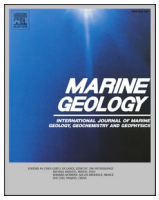

Research Article

Field observations of wave-averaged suspended sediment concentrations in the inner surf zone with varying storm conditions

P.P.J. van Wiechen *, S. de Vries, A.J.H.M. Reniers

Department of Hydraulic Engineering, Delft University of Technology, Stevinweg 1 2628 CN, Delft, The Netherlands

ARTICLE INFO

Editor: Dr. Shu Gao

Keywords:
Dune erosion
Storm surges
Suspended sediment concentrations
Surf zone
Turbulence
Surf zone currents
Pressure gradients

ABSTRACT

During extreme conditions, the transport of the wave-averaged suspended sediment concentrations in the inner surf zone affects dune erosion. Although large-scale laboratory experiments have provided insight in what drives these sediment concentrations, corresponding field data are lacking. To fill this gap, novel field observations of suspended sediment concentrations are compared to drivers that govern sediment suspension during storm conditions known from literature. A total of 128 time intervals of 20 min are analysed, spread over 10 different high water events with different hydrodynamic conditions. For each time interval, the wave-averaged (i.e. 20 min mean) suspended sediment concentration is computed and compared to three suspension drivers. The studied drivers are (1) bed shear due to near bed velocities that originate from mean currents in combination with wave-induced orbital flow, (2) the horizontal pressure gradients under steep wave fronts that increase the forces on the bed material, and (3) bore-induced turbulence that is generated at the free surface and reaches the bed. The derived bore-induced turbulence generates the greatest correlation with the mean suspended sediment concentrations ($r = 0.74$, $p = 4.47\text{E-}23$). Samples that deviate from this correlation correspond to time intervals with lower values of derived bore turbulence, less wave energy saturation in the inner surf zone, and stronger mean currents. The correlation with the mean suspended sediment concentrations increases when the shear stress originating from mean currents is used for these time intervals ($r = 0.83$, $p = 1.63\text{E-}33$). For time intervals during which more energetic conditions persist and the wave energy is saturated in the nearshore, bore turbulence was the dominant mechanism in stirring up sediment. The outcome of this study suggests that, based on the events analysed, dune erosion models may achieve more accurate results if computations of suspended sediment concentrations include a bore-induced turbulence term, or if already included, properly address the relative importance of bore-induced turbulence when compared to bed shearing.

1. Introduction

Storm conditions can lead to dune erosion and damage to coastal dune systems with loss of habitat and flooding of urban infrastructure as a consequence (Castelle et al., 2015; Masselink et al., 2016; Harley et al., 2016; Leaman et al., 2021). During storms, incident waves may collide with the dune. As a consequence, slumps of sediment slide down the dune face (van Gent et al., 2008; Palmsten and Holman, 2011, 2012). A slump that slid down will temporarily defend the dune face behind it until waves and currents mobilise the sediment from the slump and transport it offshore (van Thiel de Vries et al., 2007). After all the sediment is transported away from the dune face, the dune face is left exposed again, leaving room for a new slump to slide down. The total impact of a storm on the dune strongly depends on how fast these slumps fall down and how fast the sediment of the slump is transported offshore during the storm. The latter is influenced by the magnitude of suspended sediment concentrations in the surf zone (Steetzel, 1993; van Wiechen et al., 2023b).

Important drivers of suspended sediment concentrations in the surf zone that have been identified are (1) bed shear due to near bed velocities that originate from mean currents in combination with wave-induced orbital flow (Bailard, 1981; van Rijn, 1984; Nielsen, 1992), (2) the horizontal pressure gradients under steep wave fronts that increase the forces on the bed material (Madsen, 1975; Masselink and Puleo, 2006; van Thiel de Vries et al., 2008), and (3) bore-induced turbulence that is generated at the free surface and reaches the bed (Dally and Dean, 1984; Roelvink and Stive, 1989; Butt et al., 2004; van Thiel de Vries et al., 2008) (Fig. 1). Since all drivers occur

* Corresponding author.
E-mail address: P.P.J.vanWiechen@tudelft.nl (P.P.J. van Wiechen).

https://doi.org/10.1016/j.margeo.2024.107302
Received 11 July 2023; Received in revised form 1 May 2024; Accepted 1 May 2024
Available online 4 May 2024

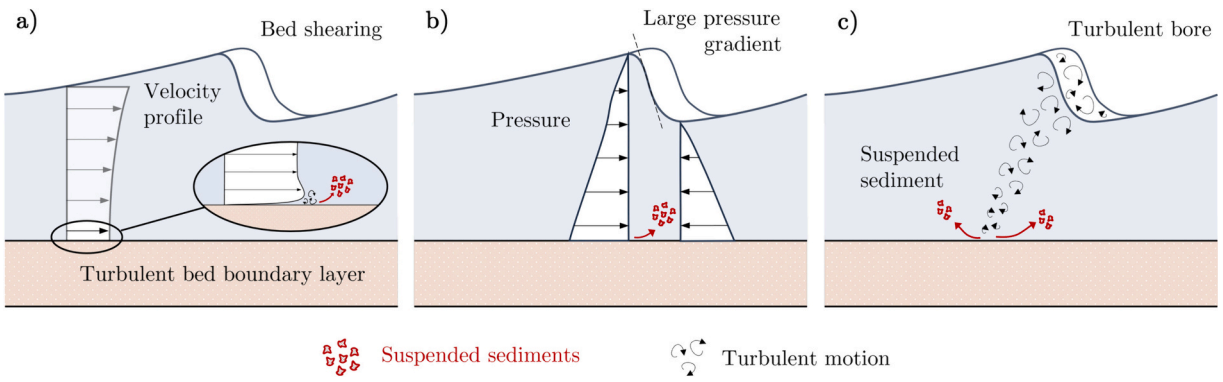

Fig. 1. Sediment suspension drivers (red arrows) that have been identified are (a) bed shear due to near bed velocities, (b) horizontal pressure gradients under steep wave fronts, and (c) bore-induced turbulence that reaches the bed. The wave is moving from left to right in each panel. (For interpretation of the references to colour in this figure legend, the reader is referred to the web version of this article.)

simultaneously during storm conditions it is difficult to differentiate between the relative magnitude and importance of each driver.

Differences in how these three drivers are implemented in model predictions translate to differences in how much sediment is predicted to be suspended in the nearshore and subsequently transported offshore (Den Heijer, 2013). For example, XBeach (Roelvink et al., 2009) includes a term accounting for both bed shearing and bore turbulence when computing the suspension of sediments (after van Thiel de Vries et al., 2008). DurosTA (Steetzel, 1993) only includes a term accounting for the dissipation of turbulent energy, which is related to bore turbulence. Under oblique wave conditions, bed shearing is expected to increase due to the generation of alongshore currents (Longuet-Higgins, 1970; Ruessink et al., 2001). As a consequence, for increasing obliquity of waves, XBeach predicts larger sediment concentrations in the nearshore and larger dune erosion volumes per unit beach width when compared to DurosTA (Den Heijer, 2013). For the normative storm conditions in the Netherlands (water level of +5 m NAP,[1] significant wave height of 9 m, peak wave period of 12 s), an incident wave angle of 40° leads to predicted erosion volumes in [m^3/m above +5 m NAP] that are 30% larger in XBeach than in DurosTA. In addition, for XBeach predictions only, the predicted erosion volumes are 30% larger for an incident wave angle of 40° when compared to normally incident waves (0°) (Den Heijer, 2013). These examples highlight the sensitivity of model predictions to formulations for suspended sediment concentrations, and the importance of proper implementation of sediment suspension drivers in dune erosion models.

Numerous wave flume experiments were conducted to study the relative magnitude and importance of sediment suspension drivers in the inner surf zone (van Rijn and Havinga, 1995; Arcilla et al., 1994; Smith and Mocke, 2002; van Thiel de Vries et al., 2008; van der Zanden et al., 2017; Eichentopf et al., 2020). Within a confined laboratory environment where the hydrodynamic forcing could be controlled, it was possible to investigate the influence of specific hydrodynamic and morphodynamic parameters individually in time. Most experiments were conducted in a 1D wave flume, and were confined to the cross-shore dimension and neglected the alongshore dimension. As a consequence, possible effects on the stirring of sediments due to 2DH processes such as an alongshore current could not be studied adequately using flumes. An exception are van Rijn and Havinga (1995), who studied oblique non-breaking waves over an ambient current. Field observations of dune erosion could provide more closure as they capture all processes naturally occurring (de Winter et al., 2015; van Bemmelen et al., 2020; Schweiger et al., 2020).

[1] Normaal Amsterdams Peil, the Dutch Chart Datum (≈ Mean Sea Level)

In this study we analyse field data to study the relative magnitude and importance of the different sediment suspension drivers on wave-averaged (corresponding to the 20 min mean) sediment concentrations (Fig. 1). The field experiment encompassed the construction of two artificial sandy dunes near the high water line with a crest height of 5.5 m NAP and crest width of 150 m (van Wiechen et al., 2024). Sediment concentrations, surface elevations, and orbital velocities were recorded continuously in the inner surf zone at both dunes for five consecutive weeks. The collected data allows a quantification of the different sediment suspension drivers for varying hydrodynamic conditions, and a comparison between variations in these drivers and variations in measured mean suspended sediment concentrations.

2. Field site and instrumentation

The data analysed in this study were collected during the RealDune/REFLEX field experiments in the autumn of 2021 and winter of 2021–2022 (van Wiechen et al., 2024; Rutten et al., 2024). In these experiments two dunes were constructed on the Sand Engine, Kijkduin, The Netherlands, with the aim of studying important processes that occur during dune erosion in the collision regime. Below, a summary is given of the segment of the field site and instrumentation that is relevant for this study. For a detailed description of the field site, instrument setup, the collected data, data accuracy and data resolution the reader is referred to van Wiechen et al. (2024) and Rutten et al. (2024). The local coordinate system and station numbers defined in van Wiechen et al. (2024) and Rutten et al. (2024) have been adopted here to remain consistent.

2.1. Field site

The two constructed dunes contained no vegetation and were constructed just above the high water line. The dunes were 150 m wide, and had a crest at an elevation of 5.5 m NAP with a width of 7 m (Fig. 2a). Dune 1 corresponds to the southern dune, Dune 2 to the northern dune. The dunes were constructed approximately 500 m apart, with differences in coastline orientation and nearshore bathymetry (Fig. 2b). These differences resulted in different nearshore hydrodynamic and morphodynamic conditions for identical offshore wave conditions.

This study involves data from the period between November 23 and December 12. Water levels within this period fluctuated between −1.24 and 2.07 m NAP. The mean low water level (MLWL) at the field site during the study period was −0.44 m NAP. The mean high water level (MHWL) at the field site during the study period was 1.25 m NAP. The mean offshore sea swell wave height was 1.28 m (at the −14.4 m NAP depth contour, see Rutten et al. (2024)). The mean offshore peak period

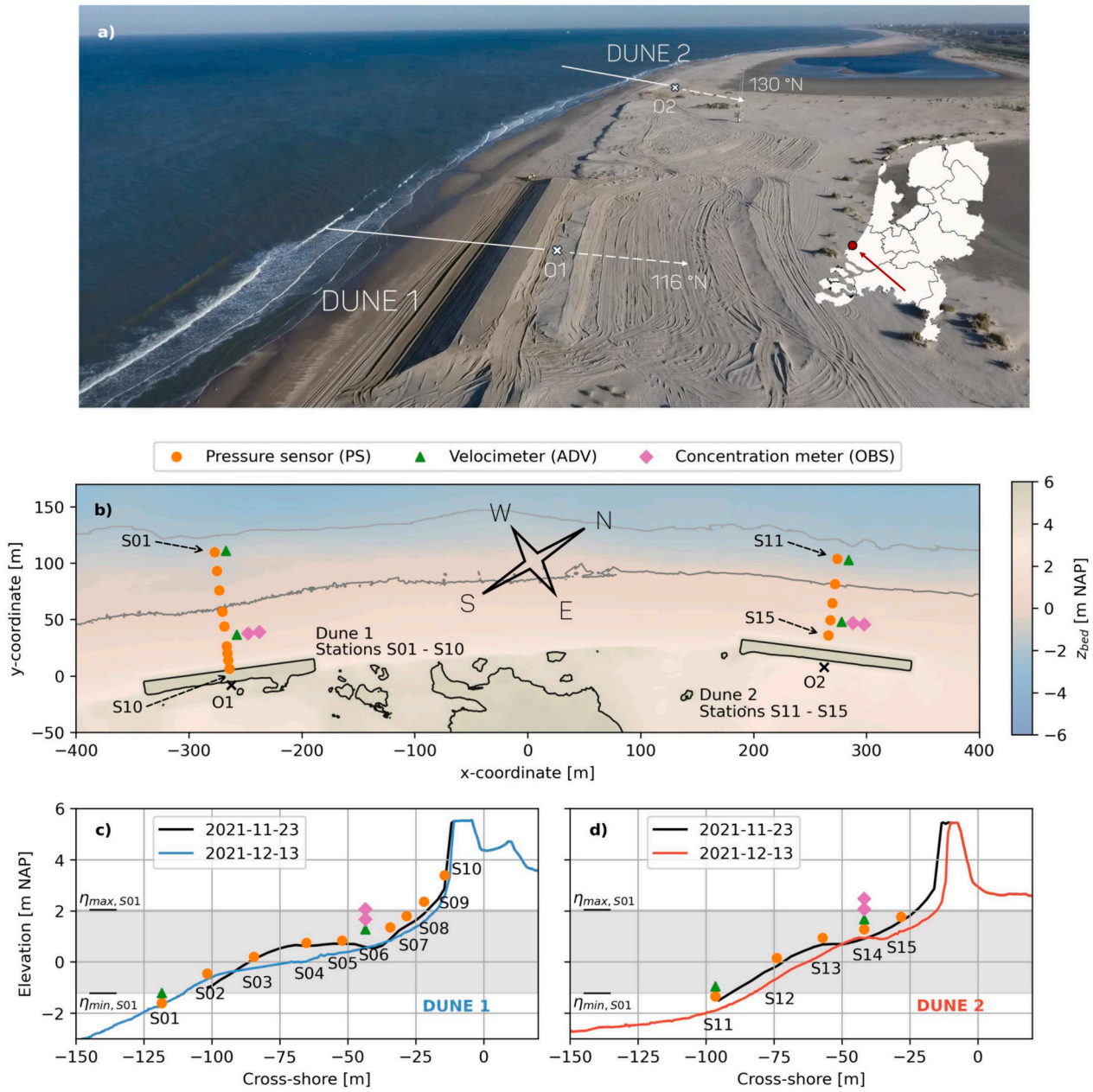

Fig. 2. a) Aerial impression of the field site including Dune 1 and Dune 2. The dashed white lines represent the positive orientations of both dunes with respect to True North. O1 and O2 represent local coordinate system origins (x-markers). b) Plan view of the instrumentation at both dunes. c-d) cross-shore instrumentation of Dune 1 (c) and Dune 2 (d). The x- and y-coordinates in b) are with respect to a temporary coordinate system to highlight the distance between both dunes. The elevations of the instruments in panels c) and d) have been changed vertically for readability and are not exactly equal to their elevations in the field. S06 had no standalone pressure sensor. Here, pressure was recorded by the built-in pressure sensor of the ADV. In panels c) and d), $\eta_{max,S01}$ and $\eta_{min,S01}$ represent the 20 min averaged maximum and minimum water levels recorded at S01 during the experiment. The Figure and captions are adopted from van Wiechen et al. (2024).

was 7.23 s. The offshore wave angle ranged from 220 to 345° true North, with a mean of 306.3° true North. Wave angles of 296° and 310° true North correspond to shore normal incidence at Dune 1 and Dune 2, respectively (Fig. 2a). One storm surge with a return period of 0.2 years occurred on December 2, and corresponds to the maximum recorded water level of 2.07 m. The maximum offshore wave height during the storm surge was 2.91 m.

The sediment from the field site was sieved in laboratory facilities to acquire information about the sediment fractions. It had a D_{10}, D_{25}, D_{50}, D_{75}, and D_{90} of respectively 236.0, 287.3, 362.3, 443.0, 557.6 μm, and can be categorised as slightly gravelly sand.

2.2. Instrumentation

Multiple sensors were used in the nearshore to measure water levels (pressures), flow velocities, and sediment concentrations (Fig. 2b-d). From November 23, 14:00 (local time) to December 12, 12:00, all sensors were successfully deployed in the field, collecting data continuously with the exception of several (short) service intervals required for changing batteries.

Pressures were recorded by RBR solo pressure sensors (RBR Global, 2022), OSSI wave gauges (Ocean Sensor Systems, 2023), and the built-in pressure sensor of the Accoustic Doppler Velocimeter (ADV, Nortek, 2018) at S06. The RBR pressure sensors (S01, S07, S08, S11, S13, S14) measured pressure at 8 Hz. The OSSI wave gauges (S02, S03, S04, S05,

S09, S10, S12, S15) measured pressure at 10 Hz. The ADV at S06 measured pressure at 16 Hz. The pressures were converted to water levels accounting for atmospheric and non-hydrostatic pressures. Flow velocities were recorded by the ADVs at S01, S06, S11, and S14. Velocities were measured in cross-shore, alongshore, and vertical direction at 16 Hz. Sediment concentrations were recorded by optical backscatter sensors (OBS, Campbell OBS3+, Campbell Scientific Inc, 2008). Two OBSs were attached to each of the ADVs at S06 and S14, and measured backscatter at 16 Hz. Within the deployment period, the height difference between the two OBSs at each ADV ranged between 0.03 and 0.09 m. The heights above the bed of the lower OBSs ranged from 0.01 m to 0.64 m. Differences in these heights were caused by the changing bathymetry of the field site. The backscatter data were converted to sediment concentrations using a calibration coefficient for each OBS. This coefficient was determined through laboratory tests. In these tests, sediment concentrations ranging from 0 to 120 g/l were generated using sediment from the field site and compared to the backscatter output of each OBS.

3. Methods

The methodology to compare measured wave-averaged sediment concentrations with different sediment suspension drivers consists of four steps. First, suitable time intervals of 20 min long are selected for analysis. The 20 min duration was assumed short enough to assume stationary hydrodynamic conditions within the interval, and long enough to allow a spectral analysis of the different frequencies within the wave signal. Second, the concentration measurements of the 20 min time intervals are filtered from outliers and contaminated data. Third, the 20 min mean of the filtered concentration timeseries are computed and converted to estimations of the mean concentrations at 0.30 m above the bed. This conversion was required to make all sediment concentrations comparable, given the changing bathymetry of the field site. The height of 0.30 m above the bed is the mean height of the OBSs of all 20 min time intervals. Fourth, the three sediment suspension drivers (Fig. 1) are quantified using the measured hydrodynamics in the inner surf zone.

3.1. Selection of events for analysis

This study will compare wave-averaged (i.e. 20 min mean) suspended sediment concentrations with sediment suspension drivers during the ten highest high waters (HWs) in the period from November 23 to December 12. The ten highest waters were identified using the mean water level at S01 (Fig. 3). The mean water level was computed using a 20 min moving average. HW5 corresponds to the high water during the storm surge on December 2. Erosion of the dune face occurred during HW4 at Dune 2, and during HW5 at both dunes.

Each HW was split into multiple 20 min time intervals around the highest water level for analysis. The mean water level during each 20 min time interval was at least 1.40 m NAP to ensure the OBSs were sufficiently submerged. The nth order spectral moments (m_n),

$$m_n = \int_0^\infty f^n E(f) \quad df, \tag{1}$$

of the detrended surface elevation timeseries, including infragravity frequencies, are used to compute the spectral (significant) wave height, H_m,

$$H_m = 4\sqrt{m_0}, \tag{2}$$

and the spectral wave period, T_m, approximated as $T_{m-1,0}$ as suggested by van Gent et al. (2008),

$$T_m = T_{m-1,0} = \frac{m_{-1}}{m_0}, \tag{3}$$

where $E(f)$ is the variance density spectrum for the different wave frequencies f of the 20 min surface elevation timeseries.

A total of 46 time intervals of 20 min were selected for each dune for further analysis. Table 1 displays the maximum mean water level (η_{max}), and the average H_m, T_m, and the mean wave direction θ_{mean} of all 20 min time intervals within each HW at S01 (Dune 1) and S11 (Dune 2). The wave direction θ_{mean} is given with respect to the shore normal of Dune 1 and Dune 2 (Fig. 2a). Negative values mean waves coming from the North-West, positive values mean waves from the South-West (see Fig. 2a and b for cardinal directions of the field site). The last column displays instruments that were not deployed during a specific HW due to service intervals.

3.2. Processing and filtering the sediment concentration measurements

The concentration timeseries of all 4 OBSs were processed and filtered for each 20 min time interval before analysis. First, all 20 min time intervals in which the OBS was not continuously above the bed

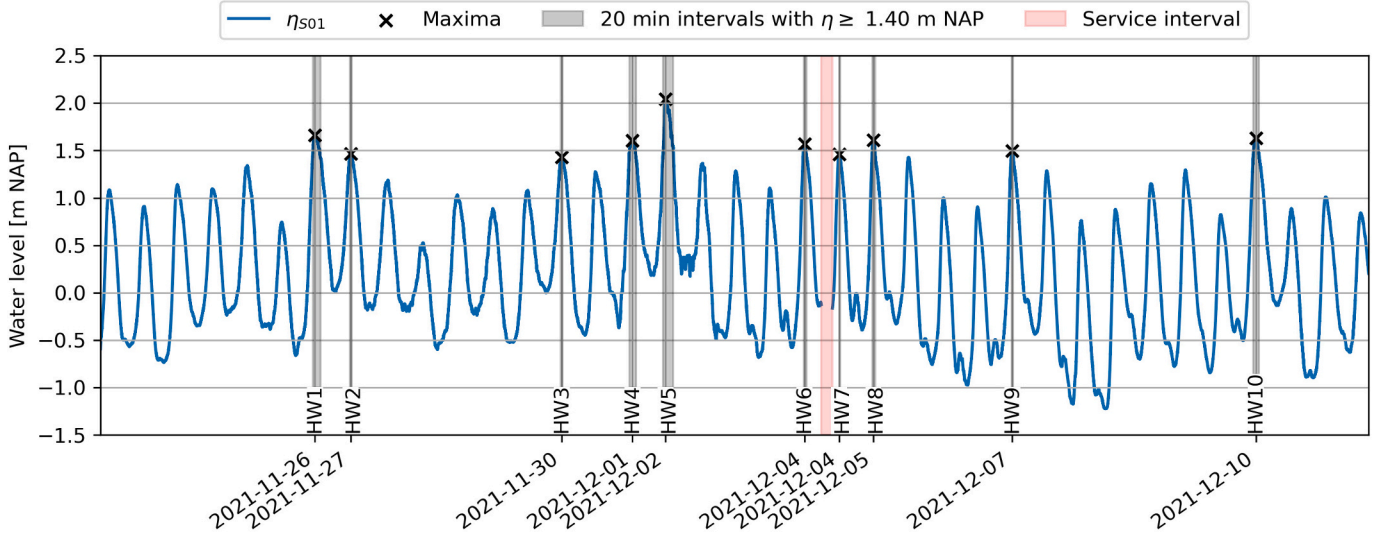

Fig. 3. Water levels at station 1 (S01) (blue), with selected time intervals for analysis based on the highest 10 HWs in the period from November 23 to December 12. (For interpretation of the references to colour in this figure legend, the reader is referred to the web version of this article.)

Table 1
Hydrodynamic conditions at S01 (Dune 1) and S11 (Dune 2) for the 10 highest HWs in the period from November 23 to December 12. The largest values for all parameters of all HWs at S01 and S11 are displayed in bold. The smallest values are displayed in italic. The wave direction is given with respect to the shore normal of the dunes. Negative values mean waves coming from the North-West, positive values mean waves from the South-West. The heights above the bed of the OBSs during each HW are given in Fig. 4.

HW	Date HW	Station	η_{max} [m]	H_m [m]	T_m [s]	θ_{mean} [°]	Non-deployed instruments
HW1	2021-11-26	S01	1.66	1.31	6.56	−5.63	
	18:45	S11	1.67	1.37	6.50	3.58	
HW2	2021-11-27	S01	1.46	1.07	7.57	−11.22	
	07:33	S11	1.46	1.29	7.33	*0.56*	
HW3	2021-11-30	S01	*1.43*	1.64	6.86	*−0.24*	ADV, OBSs at S06
	11:08	S11	1.46	1.57	6.61	8.16	
HW4	2021-12-01	S01	1.60	1.81	7.26	−0.64	
	12:24	S11	1.61	1.77	7.36	7.19	
HW5	2021-12-02	S01	**2.04**	1.75	**8.77**	**−16.17**	
	00:16	S11	**2.08**	**1.93**	**8.59**	−2.90	
HW6	2021-12-04	S01	1.57	0.84	6.66	−6.36	RBRs at S07, S08
	02:01	S11	x	x	x	3.86	RBRs at S11, S13, S14
HW7	2021-12-04	S01	1.46	*0.77*	*5.27*	−7.15	
	14:24	S11	*1.43*	*0.83*	*5.39*	5.53	
HW8	2021-12-05	S01	1.61	1.31	6.43	1.61	
	02:39	S11	1.57	1.29	6.46	**16.53**	
HW9	2021-12-07	S01	1.50	**1.88**	6.35	1.15	
	04:25	S11	1.46	1.59	6.62	10.72	ADV, OBS at S14
HW10	2021-12-10	S01	1.63	1.24	7.43	−4.39	
	19:38	S11	1.59	1.30	7.43	11.08	

were discarded (see Bs in Fig. 4a-d). The heights above the bed of the OBSs during each HW were computed using linear time interpolation of the documented heights above the bed during the LWs (low waters) surrounding each HW. The mean heights above the bed of the OBSs of each HW are displayed below panels b) and d) in Fig. 4. Second, the 20 min concentration timeseries of the OBSs that were continuously above the bed were filtered from outliers and air bubbles.

Outliers that were removed were defined as (1) NaN's (Not a Number), which indicate that the OBS output at that timestep exceeded the maximal output tested during the OBS calibration procedure, and (2) sediment concentrations larger than the mean plus 3 times the standard deviation of the concentration timeseries of the 20 min time interval. After the removal of outliers, the concentration timeseries were subjected to the air bubble filter of Smith and Mocke (2002), which is partially based on a routine of Sato et al. (1990). The filter computes the trend of the suspended sediment concentration by computing the mean of the suspended sediment concentration in the 0.3 s before a specific data point. If the specific data point is significantly higher than the mean of the previous 0.3 s, it is considered contaminated by air bubbles. The contamination threshold was set at 1.4 times the mean concentration of each time interval in this study, which is equal in a relative sense to the threshold in Smith and Mocke (2002). If the threshold is exceeded, Smith and Mocke (2002) replace the concentration data point with the mean concentration of the 0.3 s before it. In this study, the erroneous data points were discarded.

Concentration timeseries of the 20 min time intervals were kept for analysis if they still contained 80% or more of their original data points after both filters. On average, the kept timeseries still contained 93% of their original data points. There were a total of 42 concentration timeseries of 20 min suitable for analysis for the upper OBS at S06, 41 for the lower OBS at S06, 29 for the upper OBS at S14, and 26 for the lower OBS at S14 (Fig. 4a-d).

3.3. Converting sediment concentrations to an expected wave-averaged concentration at 0.30 m from the bed

The average concentration ($\overline{c}$) of the timeseries of each 20 min time interval was computed next (Figs. 4a-d and 5a). Hereafter in this paper, this 20 min averaged sediment concentration ($\overline{c}$) will be referred to as the mean suspended sediment concentration. Overall, the mean suspended sediment concentrations at S14 were larger than at S06. Mean suspended sediment concentrations within the lowest part of the water column remained within the same order of magnitude as higher up in the water column (Fig. 5a). The mean concentrations were of comparable magnitude between the upper and lower OBSs, which were approximately 0.03–0.09 m apart during the experiment (Fig. 5).

The height above the bed at which the OBSs recorded data was not constant during all HWs and 20 min time intervals (Fig. 5a). In addition, the vertical distribution of suspended sediment concentrations in the inner surf zone is known to be non-uniform (see e.g. van Rijn (1993); van Rijn and Kroon (1993); van Rijn and Havinga (1995); Steetzel (1993); Aagaard and Greenwood (2008)). To be able to compare the measured sediment concentrations between the different 20 min time intervals, $\overline{c}$ of each time interval was converted to an expected mean suspended sediment concentration at 0.30 m above the bed ($\overline{c_{0.30m}}$). The height of 0.30 m was equal to the average height above the bed of all four OBSs during all events used in the analyses (Fig. 4).

Vertical distributions of sediment concentrations under breaking waves have been subject to many studies and remain a challenge (see Aagaard et al. (2021) for a review on suspended sediment concentrations in the surf zone). Many resort to a 1DV sediment balance based on an advection-diffusion equation, discarding the horizontal advective terms (Fredsøe and Deigaard, 1992; Nielsen, 1992; Aagaard and Jensen, 2013),

$$\frac{\partial c}{\partial t} - w_s\frac{\partial c}{\partial z} - \frac{\partial}{\partial z}\left(\epsilon\frac{\partial c}{\partial z}\right) = 0, \tag{4}$$

where the sediment concentration profile is determined by the relation between the downward movement of sediment through gravity, represented by the fall velocity (w_s, [m/s]), and the up- and downward movement of sediment through the sediment diffusivity (ϵ, [m^2/s]).

In this study, we used Eq. (4) to estimate the vertical distribution of the mean suspended sediment concentrations. The first term was assumed equal to zero because we study time-averaged sediment concentrations. We assumed a constant vertical diffusivity profile for all fractions with an ϵ of 0.015 m^2/s. The constant vertical diffusivity profile suggests strong vertical mixing, starting at the near-bed region. The value of 0.015 m^2/s is equal to upper limit of ϵ in Aagaard and Jensen (2013). The assumptions of a constant vertical diffusivity profile and the value of 0.015 m^2/s are based on (1) the majority of observed

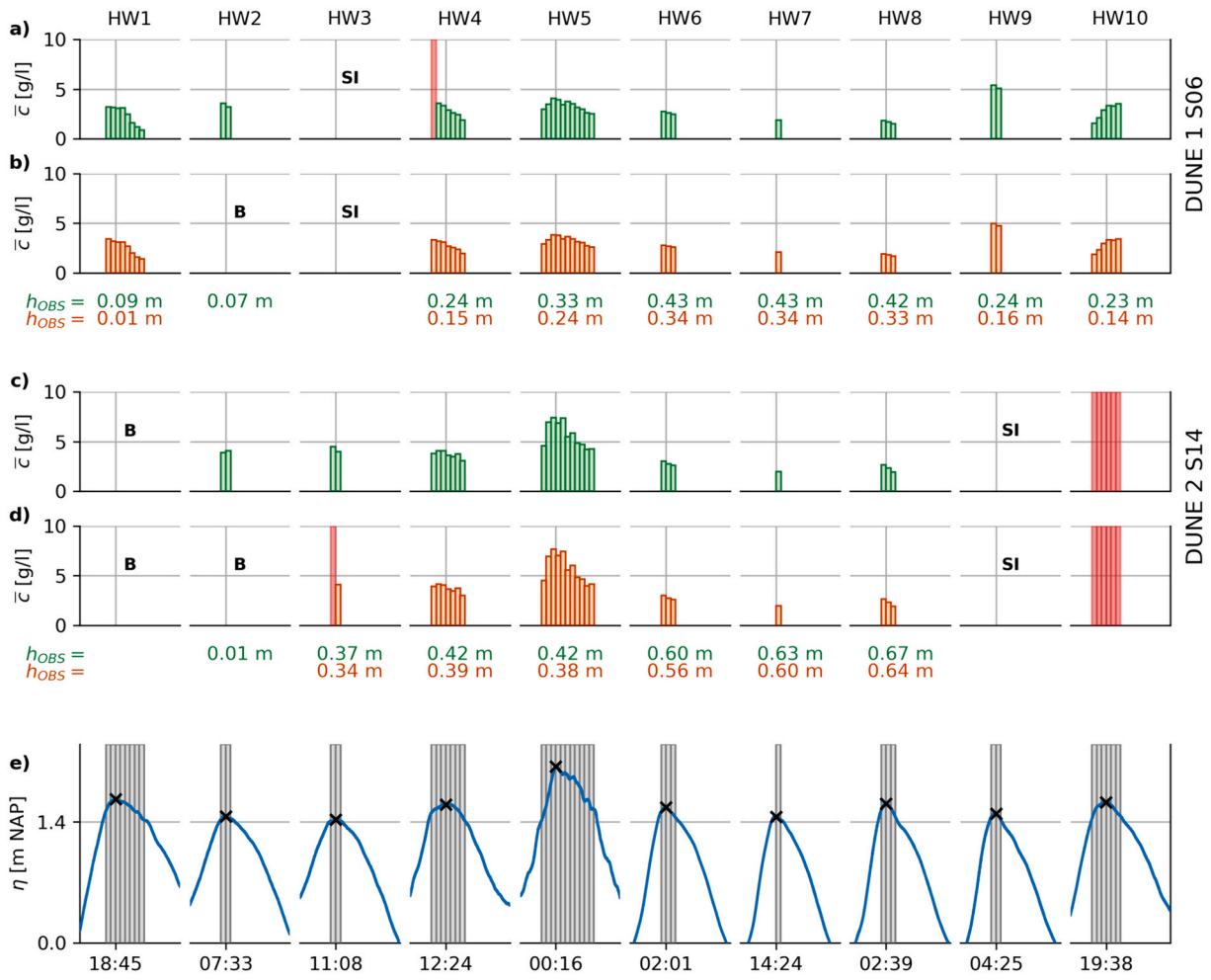

Fig. 4. Processed and filtered mean concentrations $\bar{c}$ of the (a) upper and (b) lower OBS at S06 and (c) upper and (d) lower OBS at S14, during (e) the 20 min time intervals (grey stacks). Panel e) displays the 20 min averaged surface elevation η at S01. Below panels b) and d) the mean height of the OBSs during all 20 min time intervals within each HW are displayed. Vertical red stacks in a)-d) indicate time intervals which did not contain 80% or more datapoints after application of the outlier and bubble filters. HWs during which the OBS was buried are marked with a B. HWs during which the ADV and OBSs were not deployed are marked in black with SI (service interval, Table 1). (For interpretation of the references to colour in this figure legend, the reader is referred to the web version of this article.)

waves being plunging breakers (Ogston and Sternberg, 2002; Aagaard and Jensen, 2013), (2) near-bed concentrations being of relatively equal magnitude when compared to sediment concentrations higher up in the water column (Fig. 5), and (3) wave conditions being more energetic when compared to conditions in Aagaard and Jensen (2013) (Table 1).

As a consequence, the solution to Eq. (4) is equal to (Aagaard and Jensen, 2013)

$$c(z) = C_0 exp\frac{-zw_s}{\epsilon} = \sum_{\text{fraction}=i} C_{0,i} exp\frac{-zw_{s,i}}{\epsilon}, \quad (5)$$

where C_0 is a reference concentration at the bed, and z the vertical coordinate of the water column. It is positively oriented upward and equal to 0 m at the bed.

We included five sediment fractions in our computation of $c(z)$. The total sediment concentration distribution was assumed equal to the sum of the distributions of the individual fractions (Eq. (5)). The sediment diameters of the fractions corresponded to the sediment diameters that resulted from the sieving analysis of the sediment from the field site. The fall velocities of each fraction were computed using the formula of Ahrens (2000). The fractions were included in such a way that the reference concentration at the bed consisted of 15% of sediment corresponding to the fall velocity of the D_{10}, 20% to the D_{25}, 30% to the D_{50}, 20% to the D_{75}, and 15% to the D_{90}.

Using the measured concentration by the OBS, and the known height above the bed of the OBS, the reference concentration $C_{0,i}$ was computed for all fractions for each 20 min time interval. The value of $C_{0,i}$ in combination with Eq. (5) was used to compute the expected mean suspended sediment concentration at 0.30 m from the bed $(\overline{c_{0.30m}})$.

3.4. Quantifying the three sediment suspension drivers

The three sediment suspension drivers (Fig. 1) were quantified using the measured hydrodynamics in the inner surf zone.

3.4.1. Bed shear due to mean currents and wave-induced orbital flow

The bed shear due to near bed velocities that originate from mean currents in combination with wave-induced orbital flow was quantified using the mean $(\tau_{cw,mean})$ and maximum $(\tau_{cw,max})$ bed shear stress of each 20 min time interval. These values result from a (nonlinear) combination of the current induced bed shear stress (τ_c) and the wave induced bed shear stress (τ_w) (Soulsby et al., 1993). Soulsby et al. (1993) provide simplified model parameterisations of complex hydrodynamic models (e.g. Fredsøe, 1985; Myrhaug and Slaattelid, 1990; Huynh-thanh and Temperville, 1990) to compute $\tau_{cw,mean}$ and $\tau_{cw,max}$. These parameterisations only require input for τ_c, τ_w, a current friction factor (c_f), a wave friction factor (f_w), and the angle between the mean current and

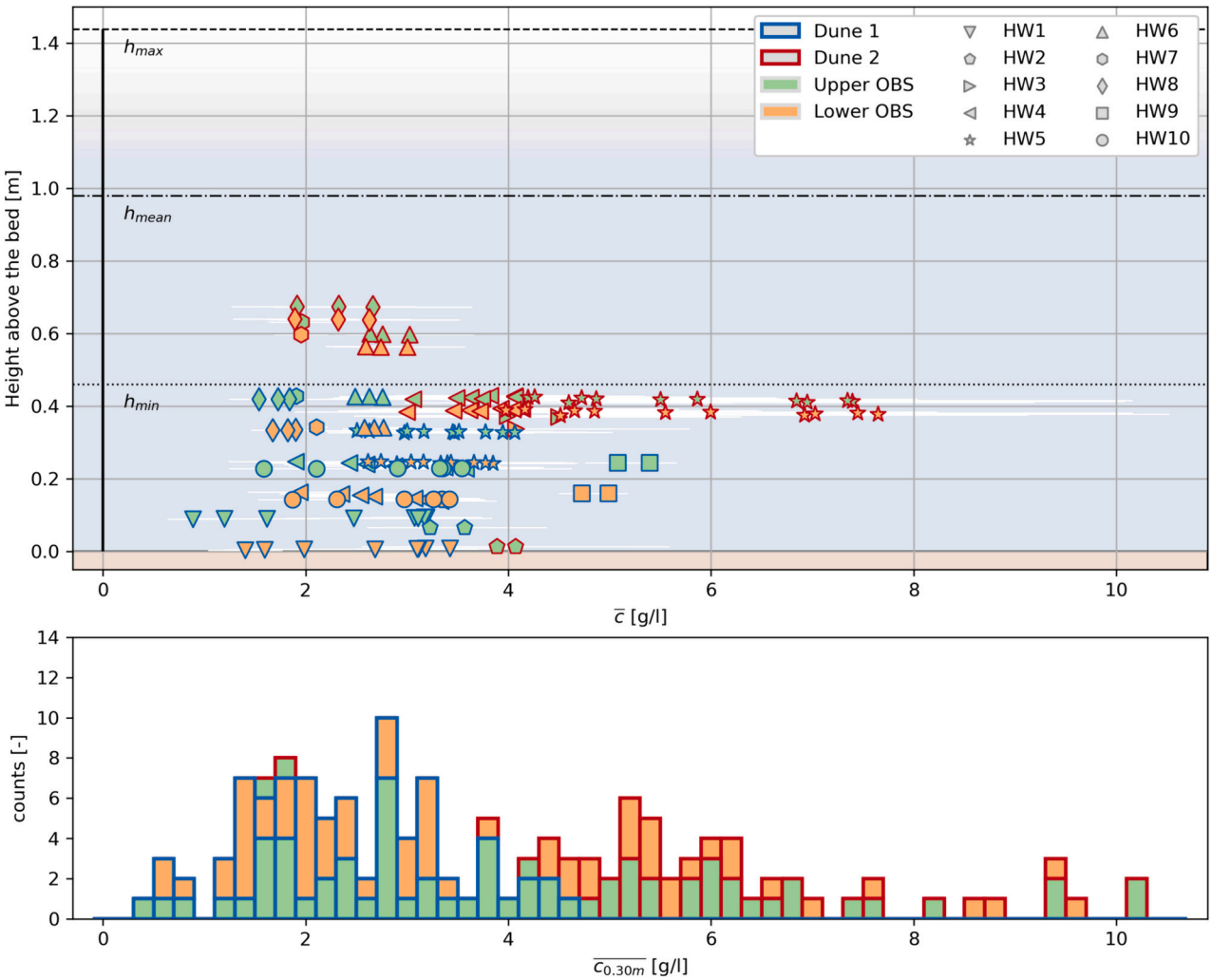

Fig. 5. a) Vertical distribution of $\overline{c}$ above the bed for all 20 min time intervals kept for analysis. Blue and red edges correspond to Dune 1 (S06) and Dune 2 (S14). Green and orange fills correspond to upper and lower OBS. The minimal, mean, and maximal water depth of all 20 min time intervals are equal to h_{min}, h_{mean}, and h_{max}. Horizontal white lines indicate ± 1 std. of the 20 min concentration timeseries. b) Histogram with 0.20 g/l bins of the expected mean suspended sediment concentration at 0.30 m above the bed ($\overline{c_{0.30m}}$). (For interpretation of the references to colour in this figure legend, the reader is referred to the web version of this article.)

the waves (φ). In this study we use Soulsby et al. (1993) with the parameterisation of Fredsøe (1985) to compute $\tau_{cw,mean}$ and $\tau_{cw,max}$. We refer to Soulsby et al. (1993) for the (constant) parameter values for Fredsøe (1985). The values of τ_c, τ_w, c_f, f_w, and φ were computed as described below.

The current induced bed shear stress (τ_c) was computed as

$$\tau_c = \rho c_f \overline{u_{da}}^2, \tag{6}$$

with ρ the density of water ($\approx$ 1025 kg/m^3), c_f a current friction factor, and $\overline{u_{da}}$ the time-averaged and depth-averaged current velocity of the 20 min time interval. The current friction factor was computed as

$$c_f = \frac{g}{C^2} \quad \text{with} \quad C = 18 log_{10} \frac{12h}{k_s}, \tag{7}$$

with C the Chézy coefficient, k_s the Nikuradse bed roughness approximated as $3D_{90}$ ($D_{90} = 557.6$ μm), and h the water depth. To compute $\overline{u_{da}}$, we assumed the current had a logarithmic profile over the vertical of the water column:

$$\overline{u_{da}} = \frac{1}{h} \int_{z=0}^{h} u(z) \partial z \quad \text{with} \quad u(z) = \frac{u_*}{\kappa} ln \frac{z}{z_0}, \tag{8}$$

with κ the von Kármán constant (= 0.41), z_0 the roughness height approximated as $k_s/33$ (Soulsby, 1998; Reniers et al., 2004b), and u_* the mean shear velocity.

The mean shear velocity was computed using the velocimeter data from the ADV. First, the velocimeter data was filtered from contaminated data by setting a beam correlation threshold for the ADV measurements, after Elgar et al. (2001, 2005). This threshold was equal to $0.3 + 0.4\sqrt{F_s/25} = 62\%$, with F_s the 16 Hz sampling frequency of the ADV. Next, the total mean current was computed as the vector sum of the mean cross-shore and alongshore current of the (filtered) ADV data. Using the total mean current at the known elevation of the ADV, u_* and subsequently $\overline{u_{da}}$ were computed following Eq. (8).

The wave induced bed shear stress was computed as

$$\tau_w = \frac{1}{2} \rho f_w \hat{u}^2, \tag{9}$$

with f_w a wave related friction factor, and $\hat{u}$ the velocity amplitude of the oscillatory flow near the bed. The correlation threshold of 62% following from Elgar et al. (2001, 2005) resulted in multiple gaps within the velocity signal of the ADV. Therefore, $\hat{u}$ was quantified by converting the timeseries of the surface elevation η at stations S06 and S14

to a timeseries of the orbital velocity u_w. The product of the wave number (k) and water depth (h) was smaller than 0.3 [−] for all 20 min time intervals at S06 and S14. Therefore, we assumed very shallow water for the conversion to u_w and a constant velocity profile over the vertical with value

$$u_w = \eta\sqrt{\frac{g}{h}}, \tag{10}$$

where g is the gravitational acceleration. The average velocity amplitude $\hat{u}$ was computed as (van der A et al., 2013)

$$\hat{u} = \sqrt{2\overline{u_w^2}}, \tag{11}$$

where the overbar denotes the time-average of u_w^2 of the 20 min time interval. The conversion from η to u_w was validated in van Wiechen et al. (2024) for a timeseries with few data gaps.

The wave related friction factor f_w was computed following Swart (1974),

$$f_w = \begin{cases} exp\left(5.213\frac{k_s}{\hat{a}}^{0.194} - 5.977\right) & \text{if} \quad \frac{k_s}{\hat{a}} < 0.63 \\ 0.3 & \text{if} \quad \frac{k_s}{\hat{a}} \geq 0.63 \end{cases}, \tag{12}$$

with $\hat{a}$ the orbital excursion amplitude of the horizontal flow, which is related to $\hat{u}$ through the spectral wave period (van der A et al., 2013):

$$\hat{a} = \frac{\hat{u}T_m}{2\pi}. \tag{13}$$

Last, φ was based on the direction of the mean current and the direction of the waves. The direction of the mean current was based on the mean cross-shore and alongshore current measured by the velocimeter. The direction of the waves was based on the velocimeter measurements that met the 62% beam-correlation threshold. Strong mean currents ($\geq$ 1 m/s) were present during HW4 at Dune 2, HW5 at Dune 1, and HW8 at Dune 2. In the presence of these strong currents, the angle between the mean current and waves was on average 76.5°.

Using Eqs. (6–13) and the computed value for φ, all required input parameters for the model of Soulsby et al. (1993) with the parameterisation of Fredsøe (1985) were computed. These parameters resulted in values for the mean $(\tau_{cw,mean})$ and maximum $(\tau_{cw,max})$ shear stress. In the comparisons with $\overline{c_{0.30m}}$, $\tau_{cw,mean}$ and $\tau_{cw,max}$ were used as a measure of the bed shear due to mean currents in combination with wave-induced orbital flow.

3.4.2. The horizontal pressure gradients under steep wave fronts

The horizontal pressure gradients under steep incident wave fronts were quantified using a characteristic wave shape in space for each 20 min time interval. The definition and computation of this characteristic wave shape in space was based on the method described in van Thiel de Vries et al. (2008). First, the characteristic wave shape is computed in the time domain using the timeseries of the surface elevation. Second, the maximum temporal gradient of the characteristic wave is computed, which is located under the wave front. Third, this maximum temporal gradient is translated to a maximum horizontal (spatial) gradient using the wave celerity of the characteristic wave, based on the linear dispersion relationship.

In the time domain, the characteristic wave shape was derived using a zero-up crossing analysis of the timeseries of the surface elevation (η), in which the up-crossing waves are rescaled and weighted summed as follows (van Thiel de Vries et al., 2008):

$$\eta_r(0:T_w) = \left(\sum_{i=1}^{i=n_{waves}} \left(\frac{H_i^2}{\sum_{i=1}^{i=n_{waves}} H_i^2} \frac{\eta(t_i:t_{i+1})}{T_i}\right)\right) T_w, \tag{14}$$

where $\eta_r(0:T_w)$ represents the characteristic wave shape in the time domain, which runs from $t = 0$ to $t = T_w$. The parameter T_w is equal to the weighted zero up-crossing wave period of the 20 min time interval,

$$T_w = \sum_{i=1}^{i=n_{waves}} \left(\frac{H_i^2}{\sum_{i=1}^{i=n_{waves}} H_i^2} T_i\right), \tag{15}$$

where weighting is based on the individual wave heights of the zero up-crossing waves (H_i). In Eqs. (14 and 15), n_{waves} is the amount of zero up-crossing waves within the 20 min timeseries of η, t_i are the timestamps of the zero up-crossings, $\eta(t_i:t_{i+1})$ are the wave shapes of the zero up-crossing waves, and T_i the wave periods of the zero up-crossing waves.

The maximum gradient in time of the characteristic wave shape $\left(\frac{\partial \eta_r}{\partial t}_{max}\right)$ is located under the wave front. This maximum gradient in time was converted to a maximum gradient in space $\left(\frac{\partial \eta_r}{\partial x}_{max}\right)$ using the celerity of the characteristic wave (c_r),

$$\frac{\partial \eta_r}{\partial x}_{max} = -\frac{1}{c_r}\frac{\partial \eta_r}{\partial t}_{max}. \tag{16}$$

The celerity of the characteristic wave shape was computed using the characteristic wave length (L_w),

$$c_r = \frac{L_w}{T_w} \tag{17}$$

which was based on T_w using the linear dispersion relationship in water depth h,

$$\left(\frac{2\pi}{T_w}\right)^2 = g\frac{2\pi}{L_w}tanh\left(\frac{2\pi}{L_w}h\right). \tag{18}$$

The absolute value of the maximum horizontal gradient $\left(\left|\frac{\partial \eta_r}{\partial x}_{max}\right|\right)$ was used as a measure of the horizontal pressure gradients under steep wave fronts in the comparisons with $\overline{c_{0.30m}}$. The absolute value was used to remove the minus sign in front of $\frac{\partial \eta_r}{\partial x}_{max}$ following from Eq. (16), and have larger (positive) pressure gradients correspond to larger and steeper waves in the inner surf zone.

3.4.3. Bore-induced turbulence that reaches the bed

The bore-induced turbulence that is generated at the free surface and reaches the bed was quantified using a 1D cross-shore energy balance in combination with a roller energy balance along the instrument arrays at both dunes. First, the energy balances were used to compute the dissipation of roller energy at S06 and S14, which was used as a proxy for the bore turbulence being generated at the free surface. Second, the dissipation of roller energy at the free surface (i.e. the bore turbulence at the free surface) was used to compute the dissipation of roller energy at the bed. Third, the dissipation of roller energy at the bed was converted to an equivalent shear stress at the bed. The shear stress at the bed was used in the comparisons with the mean concentration at 0.30 m from the bed.

The cross-shore energy balance is given by (Thornton and Guza, 1983)

$$\frac{\partial E_w c_{g,x}}{\partial x} = -\left(D_b + D_f\right), \tag{19}$$

with E_w the wave energy along the instrument array,

$$E_w = \frac{1}{8}\rho g H_{rms}^2 \tag{20}$$

where H_{rms} is the root mean squared wave height $\left(\approx H_m/\sqrt{2}\right)$. In Eq. (19), $c_{g,x}$ is the group celerity in cross-shore direction assuming shallow water $\left(\approx \sqrt{gh}\right)$, D_b the breaking-induced dissipation of wave energy,

and D_f the dissipation due to bottom friction. The breaking-induced dissipation (D_b) was modelled as (Thornton and Guza, 1983)

$$D_b = \frac{3\sqrt{\pi}}{16}\rho g B^3 \frac{H_{rms}^5}{T_m \gamma_b^2 h^3}\left[1 - \frac{1}{\left(1 + \left[\frac{H_{rms}}{\gamma_b h}\right]^2\right)^{\frac{5}{2}}}\right], \quad (21)$$

and the dissipation due to bottom friction (D_f) as (Thornton and Guza, 1983)

$$D_f = \rho f_w \frac{1}{16\sqrt{\pi}}\left(\frac{2\pi H_{rms}}{T_m sinhkh}\right)^3. \quad (22)$$

In Eqs. (21 and 22), k is the wave number ($=2\pi/L_m$) where the wave length L_m is computed using T_m and the linear dispersion relationship (Eq. (18)), and f_w is a wave-related friction factor. We assumed a constant friction factor along the instrument arrays equal to the computed values at S06 and S14 after Swart (1974) (Eq. (12)). For all 20 min time intervals, this value was approximately equal to the recommended value of 0.01 in Thornton and Guza (1983) (after Shemdin et al., 1978). The parameter γ_b is the ratio of the maximum H_{rms} over the water depth, and was computed for both dunes in this experiment using measurements of the wave height and water depth along the instrument array. Based on the wave height and water depth measurements of all 20 min time intervals, γ_b was equal to 0.55 [−] for Dune 1. For Dune 2, γ_b was equal to 0.65 [−]. The parameter B is a breaker coefficient of O(1) that accounts for differences in various breaker types. It is considered a function of the proportion of the foam region on the face of the breaker (Thornton and Guza, 1983). In this study, we use the B parameter as a calibration parameter for the model. We calibrated B for each 20 min time interval by minimising the RMSE (root mean squared error) between the measured H_{rms} and modelled H_{rms} using Eqs. (19–22) (Fig. 6a). The calibrated values of B ranged from 0.85 to 1.15 [−] for Dune 1 and 0.95–1.25 [−] for Dune 2.

The breaking-induced dissipation of wave energy (D_b) serves as a source term for the roller energy balance with roller energy E_r (Roelvink et al., 2009) (Fig. 6b),

$$\frac{\partial E_r c_{roller}}{\partial x} = D_b - D_r, \quad (23)$$

with c_{roller} the propagation speed of the roller ($\approx \sqrt{gh}$), and D_r the roller energy dissipation. The roller energy dissipation was modelled according to Reniers et al. (2004a) (Fig. 6c)

$$D_r = \frac{2g\left|\frac{\partial \eta}{\partial x_{max}}\right| E_r}{c_{roller}} \quad (24)$$

using the maximum surface slope that was computed in the previous section $\left(\left|\frac{\partial \eta}{\partial x_{max}}\right|\right)$. Eqs. (19–24) form a closed set of equations that can be solved to find roller energy dissipation at the free surface.

The roller energy dissipation at the free surface (D_r) was used to quantify the bore turbulence that was generated at the free surface. To account for the vertical decay of the bore turbulence between the free surface and the bed, D_r was multiplied with an exponential decay function after Roelvink and Stive (1989) to compute the roller energy dissipation near the bed ($D_{r,bed}$, Fig. 6c),

$$D_{r,bed} = D_r min\left(\frac{1}{exp(h/H_{rms}) - 1}, 1\right)^{\frac{3}{2}}, \quad (25)$$

where the $\frac{3}{2}$ exponent originates from the relation between the roller

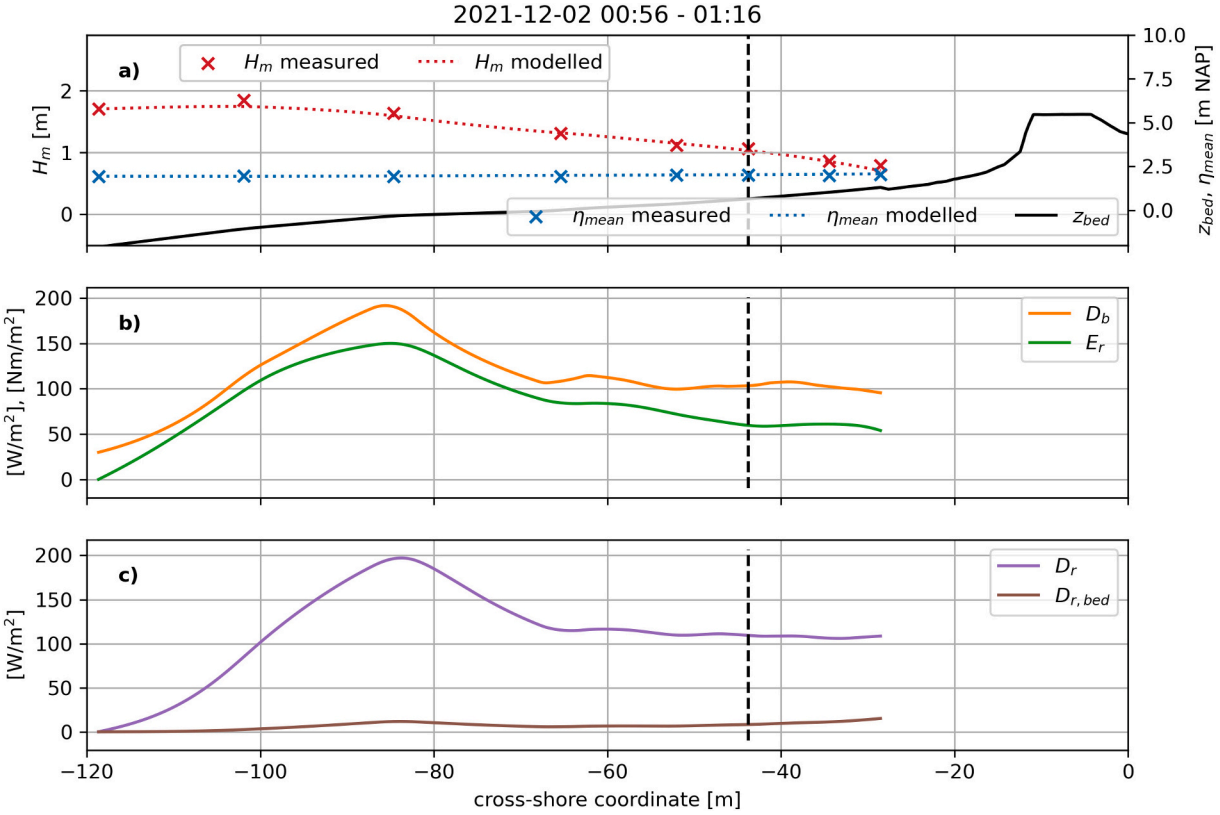

Fig. 6. Cross-shore distribution at Dune 1 during HW5 of a) the wave height and setup modelled using Eq. (19). Dotted lines represent modelled values, crosses represent instrument measurements. b) breaking-induced dissipation of wave energy (D_b, Eq. (21)) and roller energy (E_r, Eq. (23)), and c) the dissipation of roller energy (D_r, Eq. (24)) and the dissipation of roller energy near the bed ($D_{r,bed}$, Eq. (25)).

energy dissipation and the turbulent kinetic energy (k_t): $D_r \propto k_t^{\frac{3}{2}}$ (Roelvink and Stive, 1989; Reniers et al., 2013). Last, $D_{r,\mathrm{bed}}$ was converted to an equivalent shear stress through (Stive and De Vriend, 1987; Deigaard, 1993; Reniers et al., 2004b)

$$\tau_{Dr,\mathrm{bed}} = \frac{D_{r,\mathrm{bed}}}{c_{\mathrm{roller}}} = \frac{D_{r,\mathrm{bed}}}{\sqrt{gh}}. \quad (26)$$

The shear stress $(\tau_{Dr,\mathrm{bed}})$ following from the dissipation of roller energy near the bed was used as a measure for the bore turbulence reaching the bed in the comparisons with $\overline{c_{0.30\mathrm{m}}}$.

3.5. Results of the applied methods

The filtering and processing of the measured sediment concentration timeseries resulted in 138 converted mean concentrations at 0.30 m from the bed $(\overline{c_{0.30\mathrm{m}}})$. During HW2, the ADVs at S06 and S14 were too close to the bed to yield accurate velocity measurements. During HW6, the RBR at S14 had a service interval. As a consequence, not all three sediment suspension drivers could be quantified for the 20 min time intervals during HW2 at S06 and S14 and during HW6 at S14. These 20 min time intervals were excluded from the analyses. This ultimately brought the total amount of mean concentrations at 0.30 m from the bed $(\overline{c_{0.30\mathrm{m}}})$ fit for comparisons to 128. These 128 values were compared to the three suspension drivers, quantified by $\tau_{\mathrm{cw,mean}}$ and $\tau_{\mathrm{cw},max}$, $|\frac{\partial \eta}{\partial x}_{\mathrm{max}}|$, and $\tau_{Dr,\mathrm{bed}}$.

4. Results and analysis

Fig. 7 displays the results of the comparisons between $\overline{c_{0.30\mathrm{m}}}$ and the parameters used to quantify the three sediment suspension drivers. For each comparison, r represents the Pearson correlation coefficient and p the associated p-value.

The mean bed shear stress induced by mean currents and wave-orbital velocities $(\tau_{\mathrm{cw,mean}})$ showed no correlation with $\overline{c_{0.30\mathrm{m}}}$ (Fig. 7a, $r = 0.13$, $p = 1.36\mathrm{E}{-01}$). The largest values of $\tau_{\mathrm{cw,mean}}$ were found for HW4 at Dune 2, HW5 at Dune 1, and HW8 at Dune 2. These HWs had a relatively large angle of wave incidence (Table 1), which likely caused strong alongshore currents ($\geq$ 1 m/s) and consequently large shear stresses. These larger shear stresses did not necessarily result in larger

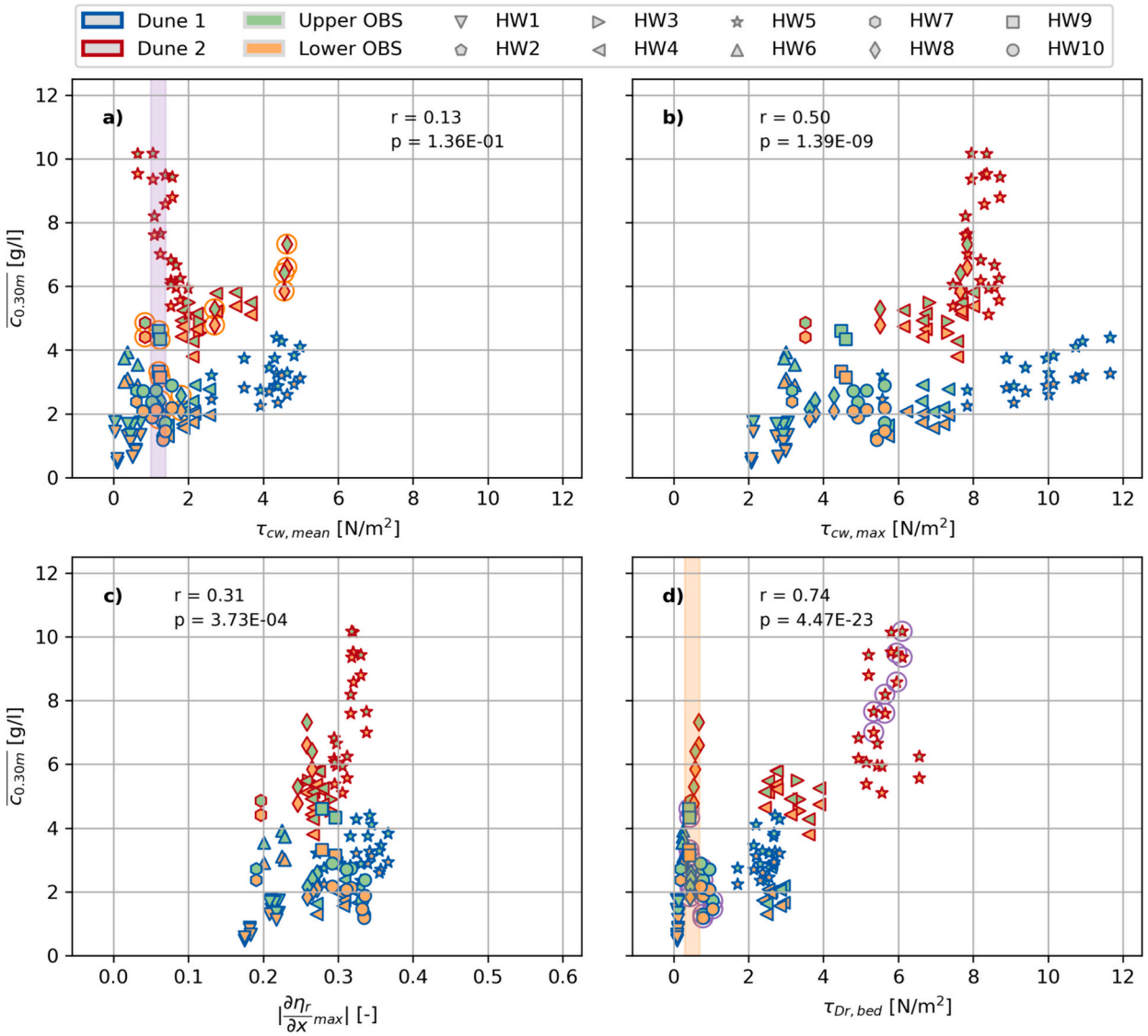

Fig. 7. Comparison between $\overline{c_{0.30\mathrm{m}}}$ and a) $\tau_{\mathrm{cw,mean}}$, b) $\tau_{\mathrm{cw},max}$, c) $|\frac{\partial \eta_r}{\partial x}_{\mathrm{max}}|$, and d) $\tau_{Dr,\mathrm{bed}}$. The r and p values correspond to the Pearson correlation coefficient and p-value. Blue and red edges correspond to Dune 1 (S06) and Dune 2 (S14). Green and orange fills correspond to upper and lower OBS. (For interpretation of the references to colour in this figure legend, the reader is referred to the web version of this article.)

sediment concentrations. Values of $\tau_{cw,mean}$ were similar between HW5 at Dune 2, and HW8, HW9 and HW10 at Dune 1. However, the spread in measured concentrations was large (vertical purple bar in Fig. 7a). The maximum bed shear stress $(\tau_{cw,max})$ showed some correlation with $\overline{c_{0.30m}}$ (Fig. 7b, $r = 0.50$, $p = 1.39E\text{-}09$). The spread of $\overline{c_{0.30m}}$ was larger for larger values of $\tau_{cw,max}$ (≥ 6 N/m^2). These larger values were a result from both larger mean currents, and larger orbital velocities due to relatively more energetic wave conditions (e.g. HW5 at Dune 1 and Dune 2).

The measure for the horizontal pressure gradients under steep wave fronts $\left(\left|\frac{\partial \eta_L}{\partial x_{max}}\right|\right)$ showed no correlation with $\overline{c_{0.30m}}$ (Fig. 7c, $r = 0.31$, $p = 3.73E\text{-}04$). A possible explanation for this absent correlation is that this parameter can be interpreted as a parameter that became larger when waves started shoaling, and reached a maximum when they were breaking. During events with larger offshore wave heights (e.g. HW4, HW5), this upper limit was reached, which was somewhere between 0.3 and 0.4 [−]. As a consequence of this upper limit, there was no further distinction in $|\frac{\partial \eta_L}{\partial x_{max}}|$ between the different 20 min time intervals within the more energetic HWs. However, there was a difference in measured sediment concentrations within these more energetic HWs, especially between Dune 1 and Dune 2 (Fig. 7c).

The shear stress following from the roller energy dissipation reaching the bed $(\tau_{Dr,bed})$, representing the bore turbulence, showed the greatest correlation with $\overline{c_{0.30m}}$ (Fig. 7d, $r = 0.74$, $p = 4.47E\text{-}23$). The 20 min time intervals during HW7 and HW8 at Dune 2, and HW9 at Dune 1 deviated from the correlation (vertical orange bar in Fig. 7d).

The 20 min time intervals that deviated from the correlation had similar values of $\tau_{Dr,bed}$, but large differences in $\overline{c_{0.30m}}$. The values of $\tau_{Dr,bed}$ for these HWs were generally low (orange bar Fig. 7d). These time intervals displayed larger differences in $\tau_{cw,mean}$ (orange encircled markers in Fig. 7a). Contrarily, for smaller values of $\tau_{cw,mean}$, there was a substantial spread in $\overline{c_{0.30m}}$ (purple bar Fig. 7a). The 20 min time intervals corresponding to this larger spread are marked with purple circles in Fig. 7d, and displayed larger differences in $\tau_{Dr,bed}$. The parameter $\tau_{cw,mean}$ is current related and does not include the wave-related motion (these are included in $\tau_{cw,max}$). The parameter $\tau_{Dr,bed}$ primarily includes shear stresses related to wave breaking and does not include current related shear stresses. These observations suggest that sediment concentrations were dominated by mean currents when the magnitude of the bore-related turbulence was low, and vice versa.

The dominance by either mean currents or bore related turbulence was studied in more detail by computing the relative magnitude α of the bore induced shear stress to the current-related shear stress through

$$\alpha = \frac{\tau_{Dr,bed}}{\tau_{Dr,bed} + \tau_{cw,mean}}, \tag{27}$$

where α runs from 0 (current shear dominated) to 1 (bore turbulence

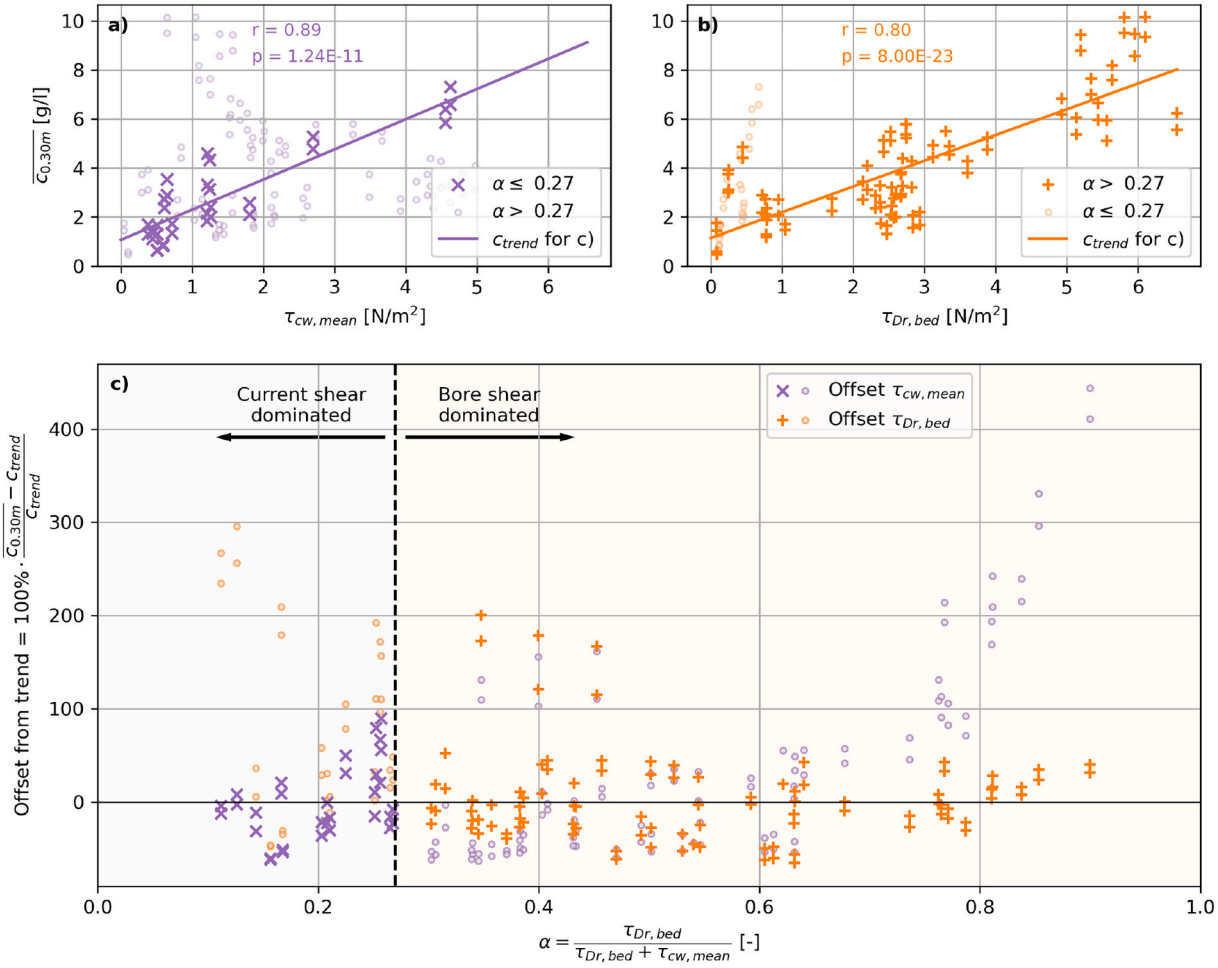

Fig. 8. a) Data points of Fig. 7a, where markers are crosses when $\alpha \leq 0.27$ (Eq. (27)). b) Data points of Fig. 7d, where markers are pluses when $\alpha > 0.27$. The lines are the best linear fits through the crosses and pluses, representing the trend of the relation between $\overline{c_{0.30m}}$ and $\tau_{cw,mean}$ and $\tau_{Dr,bed}$. c) Offset in percentage of the data points with respect to the trends in panels a) (purple) and b) (orange), computed as $100\% \cdot (\overline{c_{0.30m}} - c_{trend})/c_{trend}$. The offsets of panel a) become large for $\alpha \gg 0.27$ (purple dots in the right), i.e. when $\tau_{Dr,bed}$ dominates over $\tau_{cw,mean}$, and vice versa for panel b) (orange dots in the left). (For interpretation of the references to colour in this figure legend, the reader is referred to the web version of this article.)

shear dominated). Points that deviated more strongly from the correlation between $\overline{c_{0.30m}}$ and $\tau_{Dr,bed}$ (e.g. orange bar in Fig. 7d) corresponded to low values of α. Contrarily, points that deviated from the correlation between $\overline{c_{0.30m}}$ and $\tau_{cw,mean}$ (e.g. purple bar in Fig. 7a) corresponded to high values of α (Fig. 8c).

For α-values up or equal to 0.27 [−], the current shear stress appeared to correlate better to mean suspended sediment concentrations (Fig. 8a, c). When α became larger than 0.27 [−], the bore turbulence shear correlated better to mean suspended sediment concentrations (Fig. 8b, c). When we define a single shear stress (τ_{comb}) in which we separate the contribution of either $\tau_{cw,mean}$ or $\tau_{Dr,bed}$ based on their relative contribution through α,

$$\tau_{comb} = \begin{pmatrix} \tau_{cw,mean} & \text{if} \quad \alpha \leq 0.27 \\ \tau_{Dr,bed} & \text{if} \quad \alpha > 0.27 \end{pmatrix}, \tag{28}$$

the largest overall correlation with $\overline{c_{0.30m}}$ is found (Fig. 9, $r = 0.83$, $p = 1.63E\text{-}33$). The correlation was smaller for all other α-values used as a boundary between $\tau_{cw,mean}$ and $\tau_{Dr,bed}$ (i.e. $\alpha \neq 0.27$).

Possible combinations of $\tau_{cw,mean}$ and $\tau_{Dr,bed}$ (e.g. the (weighted) sum) were also tested. However, no combination resulted in a larger correlation than the one found for τ_{comb} computed with Eq. (28).

The correlation between τ_{comb} and $\overline{c_{0.30m}}$ is larger than the correlations of the individual suspension drivers in Fig. 7. This supports the suggestion that sediment concentrations can be dominated by current shear stresses when wave-related stresses are low, and vice versa. Of all 128 values of $\overline{c_{0.30m}}$ used in the comparisons, 32 values were dominated by $\tau_{cw,mean}$ (i.e. $\alpha \leq 0.27$). The 20 min time intervals corresponding to these values were during HW1 (S06), HW6 (S06), HW7 (S06), HW8 (S06 and S14), and HW9 (S06).

On average, the hydrodynamic conditions were more energetic at S06 and S14 during the 96 20 min time intervals in which $\tau_{Dr,bed}$ dominated: the average H_m of the 96 intervals was 0.85 m (against 0.57 m for the other 32 intervals), the average T_m was 12.90 s (against 11.16 s), the average water level was 1.72 m NAP (against 1.65 m NAP), and the average water depth 1.06 m (against 0.96 m).

The wave height over water depth ratio (H_m/h) can be interpreted as a measure for the degree of wave energy saturation due to wave breaking in the inner surf zone (Battjes and Janssen, 1978; Thornton and Guza, 1983). For the 20 min time intervals in which $\tau_{Dr,bed}$ dominated, the average ratio was equal to 0.80. The average ratio was equal to 0.60 for the 20 min time intervals in which $\tau_{cw,mean}$ dominated. The magnitude and difference in magnitude of the ratios suggests that (a) almost all waves are breaking in the bore turbulence dominated 20 min time intervals, and (b) the attenuation of the bore turbulence between being generated at the free surface and reaching the bed is less for the bore turbulence dominated 20 min time intervals when compared to the current dominated 20 min time intervals (see dependence in Eq. (25)). These results suggest that when more energetic conditions persisted and wave energy became fully saturated in the inner surf zone, bore turbulence was likely to become the dominant mechanism in suspending sediment.

5. Discussion

5.1. Measured sediment concentrations

The elevation above the bed at which the OBSs measured suspended sediment concentrations varied throughout the experiment. To be able to compare concentration measurements at different elevations between different events, a sediment balance based on a 1D vertical advection diffusion equation was set up (Eq. (4)). Measured mean concentrations were converted to an expected elevation of 0.30 m above the bed. This balance did not include the horizontal advection and diffusion terms (both in cross-shore and alongshore direction). Because sediment concentrations were recorded at only one location within the horizontal plane, a data-based quantification of these horizontal terms was not possible. Possible effects of the horizontal advection and diffusion terms on the variability of measured sediment concentrations in the inner surf zone can therefore not be excluded.

An important term in the 1D vertical advection diffusion equation is the sediment diffusivity (ϵ). The value of ϵ determines the degree of vertical mixing, and has a strong influence on the vertical distribution of the mean suspended sediment concentration. As a consequence, the expected concentration at 0.30 m from the bed strongly depends on the value of ϵ. A constant diffusivity profile (in time and space) over the vertical was assumed with a value of 0.015 m^2/s. This assumption was based on the similarities in field site and wave conditions between this study and Aagaard and Jensen (2013), and the vertical distribution of the measured, non-converted, sediment concentrations (Fig. 5a).

We want to highlight the sensitivity of the results of this study to the choice of ϵ: Larger values of ϵ would result in a more linear instead of logarithmic profile, and hence to smaller differences over the vertical between sediment concentrations. By converting all concentration

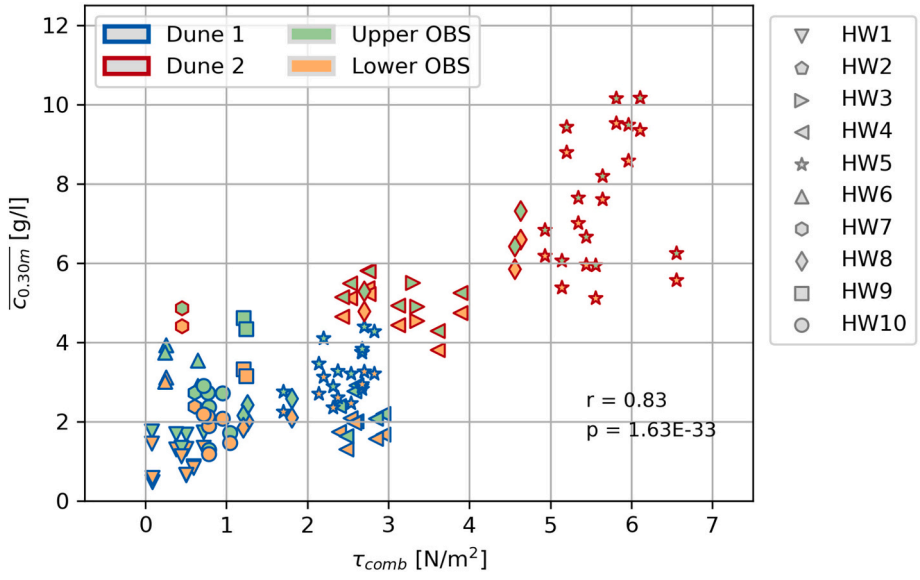

Fig. 9. Comparison between $\overline{c_{0.30m}}$ and τ_{comb} for $\alpha = 0.27$ [−] (Eqs. (27 and 28)).

Table 2
Unconverted and converted mean suspended sediment concentrations with different values of ϵ (0.010, 0.015 and 0.020 m^2/s). The first and third row correspond to events with the lowest and highest elevation above the bed of the OBS (z_{obs}) throughout the experiment.

Event	z_{obs} [m]	$\overline{c}$ [g/l]	$\overline{c_{0.30m}}$ [g/l] 0.010 m^2/s	$\overline{c_{0.30m}}$ [g/l] 0.015 m^2/s	$\overline{c_{0.30m}}$ [g/l] 0.020 m^2/s
HW1 S06 18:05–18:25	0.01	3.42	0.97	1.45	1.78
HW5 S14 00:16–00:36	0.38	7.03	9.70	8.80	8.35
HW8 S14 02:19–02:39	0.67	2.66	11.18	7.32	5.82

measurements to a height equal to the mean height above the bed of all OBSs, the sensitivity to ϵ of all measurements was kept to a minimum. Nevertheless, the sensitivity to values of ϵ remained substantial for 20 min time intervals in which the height above the bed of the OBS was substantially different from 0.30 m (Table 2).

When no conversion is performed on the measured suspended sediment concentrations and $\overline{c}$ is used in the comparisons, the r correlation coefficients of panels a, b, c, and d in Fig. 7 become 0.00, 0.47, 0.45, and 0.75, respectively. The associated p-values are 9.56E-01, 1.48E-08, 1.07E-07, and 1.85E-24, respectively. This means the correlation for the term related to the modelled shear stress following from bore turbulence remains largest, and interestingly enough, (slightly) increases. No τ_{comb} could be generated based on Eq. (28) that resulted in a larger correlation with $\overline{c}$ than the one associated to $\tau_{Dr,bed}$. This means that the largest overall correlation remains between τ_{comb} and $\overline{c_{0.30m}}$ ($r = 0.83$ and $p = 1.63E\text{-}33$, Fig. 9).

The difference in r-values between the unconverted ($\overline{c}$) and converted ($\overline{c_{0.30m}}$) mean suspended sediment concentrations and $\tau_{Dr,bed}$ likely originates from the small difference in measured concentrations between the upper and lower OBS at S06 and S14 (Figs. 4 and 5). The measured differences between the upper and lower OBSs were smaller than the expected differences between the upper and lower OBSs based on the solution of the 1D vertical advection diffusion equation (Eq. (5)). As a consequence, the conversion from $\overline{c}$ to $\overline{c_{0.30m}}$ introduces a (small) offset between the upper and lower OBS at S06 and S14 and hence a (slightly) smaller r value (0.74 versus 0.75).

5.2. Assumptions in quantifying nearshore hydrodynamics

The parameters quantifying the bed shearing, $\tau_{cw,mean}$ and $\tau_{cw,max}$, were computed following Swart (1974), Fredsøe (1985) and Soulsby et al. (1993), accounting for wave orbital flow with a superimposed mean current. The superimposed mean current was estimated using data from the ADVs at S06 and S14, which was converted to an estimate of the depth-averaged current velocity assuming a logarithmic velocity profile. The orbital flow was estimated by converting water level measurements at the location of the ADVs to an orbital velocity using shallow water linear wave theory.

The horizontal pressure gradients under steep incident wave fronts were quantified using the maximum spatial gradient of the characteristic wave shape for each 20 min time interval $\left(\left|\frac{\partial \eta_r}{\partial x}_{max}\right|\right)$. The definition and computation of this characteristic wave shape in space were based on the method of van Thiel de Vries et al. (2008). The values of $\left|\frac{\partial \eta_r}{\partial x}_{max}\right|$ ranged between 0.17 and 0.38 [−] at S06 and S14, corresponding to wave fronts with surface slope angles ranging from 9.65 to 20.75°. These values are in accordance with observed values in Duncan (1981) and Yang et al. (2022), and below observed values of the surface slope angle at the point of wave overturning (Feddersen et al., 2023).

The bore induced turbulence was quantified by modelling the dissipation of roller energy (D_r) using a 1D cross-shore energy balance in combination with a roller energy balance (following Thornton and Guza, 1983; Reniers et al., 2004a; Roelvink et al., 2009). Wave height and nearshore water levels were modelled using Eqs. (19–22), where the parameter B was used to calibrate the model. On average, the RMSEs (root mean squared error) of the modelled and measured root mean squared wave heights were 0.04 m for both Dune 1 (S01 - S06) and Dune 2 (S11 - S14) (see Fig. 6 for an example 20 min time interval). The RMSEs of the modelled and measured water levels were 0.03 m for Dune 1 and 0.10 m for Dune 2. The slightly larger offset of the modelled water level at Dune 2 was likely due to a portion of water being able to flow around the northern edge Dune 2 at the field site (Fig. 2), reducing the total wave setup. The modelled dissipation of roller energy could not be validated with measurements, and is therefore subject to its own uncertainties following Reniers et al. (2004a) and Roelvink et al. (2009).

5.3. Sediment concentrations and dune erosion in the collision regime

This study focused on the 10 highest high waters (HWs) in the period from November 23 to December 12, based on the water level data at S01 (Fig. 3, Table 1). Of these HWs, two resulted in dune erosion in the collision regime. On December 1, slumping of the dune face occurred at Dune 2. On December 2, slumping occurred at Dune 1 and Dune 2.

The measured sediment concentrations by the OBSs in the inner surf zone were not significantly higher during the HWs with dune erosion in the collision regime. This means that the slumps that slid down the dune face did not seem to influence the measurements of sediment concentrations at stations S06 and S14. On December 1, during HW4, sediment concentrations at S14 in front of Dune 2 were of comparable magnitude when compared to HW2 and HW3. On December 2 (HW5), sediment concentrations recorded at S06 in front of Dune 1 were of comparable magnitude when compared to HW1, HW2, HW4, HW9 and HW10. It is noted, however, that the measured sediment concentrations were at approximately 30 m from the dune face. There may be larger differences in sediment concentrations in closer proximity to the dune.

5.4. Implications for process-based dune erosion models

Existing process-based dune erosion models use different formulae to compute the suspension of sediments in the inner surf zone. These formulae are developed using different physical processes as a basis, which possibly result in differences in model predictions under varying surge levels and wave conditions (Den Heijer, 2013).

This study showed that, for the events analysed and compared here, mean currents and modelled bore turbulence contributed both to the suspension of sediments and the magnitude of the mean suspended sediment concentrations in the inner surf zone. When more energetic (storm) conditions persisted and wave energy became saturated in the inner surf zone (i.e. large wave height to water depth ratios), the modelled bore turbulence correlated best and became the more dominant suspension driver. Such conditions are more likely to occur during dune erosion in the collision regime.

These findings suggest that model approximations of dune erosion in the collision regime could achieve more accurate results if computations of suspended sediment concentrations include a bore-induced turbulence term, which could be added to more conventional sediment suspension formulations using flow-induced bed shearing (e.g. van Rijn

(1993); Soulsby (1998)). In addition, models in which flow-induced bed shearing and bore turbulence are both included in the sediment concentration computation (e.g. XBeach, Roelvink et al., 2009), more accurate results can be achieved when the relative contribution of bore turbulence to suspended sediment concentrations is properly implemented. For the cases studied here, the relative contribution of bore turbulence depended on the degree of energy saturation in the inner surf zone. The wave height to water depth ratio appeared to be a good indicator of when the relative contribution of bore turbulence to suspended sediment concentrations increased, and when it potentially dominated over the contribution of flow-induced bed shearing due to mean currents.

6. Conclusions

A prototype-scale field experiment was conducted to study sediment suspension drivers in the inner surf zone with varying storm surge levels. A total of 128 time intervals of 20 min were analysed. These intervals were spread over 10 different high water events with different hydrodynamic conditions. For each 20 min time interval, the wave averaged suspended sediment concentration was computed. The concentration measurements were performed at different heights above the bed throughout the experiment. Therefore, the mean concentration of each 20 min time interval was converted to an estimated mean suspended sediment concentration at 0.30 m from the bed. This estimation was compared to three sediment suspension drivers known from literature. The studied drivers were (1) bed shear due to near bed velocities that originate from mean currents in combination with wave-induced orbital flow, (2) the horizontal pressure gradients under steep wave fronts that increase the forces on the bed material, and (3) bore-induced turbulence that is generated at the free surface and reaches the bed.

When all three drivers were compared individually with the measured mean suspended sediment concentrations, the derived shear stresses following from bore-induced turbulence showed the largest correlation ($r = 0.74$, $p = 4.47\text{E-}23$). Samples that deviated from this correlation corresponded to 32 time intervals with lower values of derived bore turbulence and stronger mean currents. The correlation with the mean suspended sediment concentrations increased when the derived shear stress originating from mean currents was used for these 32 less energetic time intervals, and the derived shear stress following from bore-induced turbulence was used for the other 96 more energetic time intervals ($r = 0.83$, $p = 1.63\text{E-}33$). Overall, for time intervals during which more energetic conditions persisted and the wave energy was saturated in the nearshore, bore turbulence was the dominant mechanism in stirring up sediment. For these time intervals, almost all waves were breaking and contributed to the generation of bore turbulence at the free surface. In addition, the generated turbulence at the free surface was attenuated less before reaching the bed, resulting in relatively large shear stresses at the bed.

For the events analysed and compared here, the results suggest that mean currents and bore turbulence contributed both to the suspension of sediments and the magnitude of the mean suspended sediment concentrations in the inner surf zone. When wave conditions were more energetic (i.e. storm conditions) and the wave energy in the inner surf zone was saturated, the derived shear stresses following from bore turbulence correlated better to measured suspended sediment concentrations. These findings suggest that model approximations of dune erosion could achieve more accurate results if computations of suspended sediment concentrations include a bore-induced turbulence term. This term could be added to conventional sediment suspension formulations using flow-induced bed shear. If a bore-induced turbulence term is added to model formulations using flow-induced bed shear, the relative contribution of the bore-induced turbulence term with respect to the flow-induced bed shear terms should be properly implemented. In this study, the relative contribution of bore turbulence depended on the degree of energy saturation in the inner surf zone. The wave height to water depth ratio appeared to be a good indicator of when the relative contribution of bore turbulence to suspended sediment concentrations increased, and when it potentially dominated over the contribution of bed shearing due to mean currents.

Open research section

All data supporting the conclusions are published with open access on the 4TU.ResearchData repository (van Wiechen et al., 2023a) with doi:

doi:https://doi.org/10.4121/0a05d041-00b6-4e8e-a5c5-70e624ea720b

The data are stored as a data collection with name'Nearshore coastal measurements of calm, moderate, and storm conditions at two artificial dunes along the Dutch Coast during the RealDune/REFLEX experiments'. An accompanying data paper was published in Scientific Data (van Wiechen et al., 2024). The offshore data used in the site description are from Rutten et al. (2024).

CRediT authorship contribution statement

P.P.J. van Wiechen: Conceptualization, Data curation, Formal analysis, Investigation, Methodology, Software, Validation, Visualization, Writing – original draft, Writing – review & editing. **S. de Vries:** Conceptualization, Data curation, Formal analysis, Funding acquisition, Methodology, Project administration, Resources, Supervision, Visualization, Writing – original draft, Writing – review & editing. **A.J.H.M. Reniers:** Formal analysis, Funding acquisition, Methodology, Supervision, Validation, Writing – original draft, Writing – review & editing.

Declaration of competing interest

The authors declare that they have no known competing financial interests or personal relationships that could have appeared to influence the work reported in this paper.

Acknowledgements

The authors would like to thank dr. Jantien Rutten and dr. Marion Tissier for their continuous support in designing, constructing, and monitoring the field site. They thank the technicians Pieter van der Gaag, Arie van der Vlies, and Arno Doorn of Delft University of Technology for their contributions in the preparation and execution of the experiments, and the technician Marcel van Maarseveen of University of Utrecht for the detailed OBS calibrations conducted in the university lab facilities. The authors also like to thank the anonymous reviewers for their clear, constructive, and detailed comments.

This study is part of the RealDune and REFLEX projects. These projects are part of a larger framework to re-evaluate the hydrodynamic and morphodynamic processes that play a role in the national safety assessment of sandy coastlines in the Netherlands. Both projects are TKI (Topconsortia for Knowledge and Innovation) Delta Technology projects, and receive additional funding from TKI Delta Technology to stimulate collaboration between government institutes, knowledge institutes, and businesses specialised in the field of Hydraulic Engineering. The RealDune consortium exists out of Delft University of Technology, Rijkswaterstaat (the Dutch Ministry of Infrastructure and Water Management), STOWA (the Dutch Waterboards), Deltares, Arcadis, and Witteveen + Bos. The REFLEX consortium exists out of Delft University of Technology, Rijkswaterstaat, Deltares, Stichting Zawabas, Witteveen + Bos, Arcadis, and Nortek. The dunes of the experiment were constructed by Boskalis. The sediment sieving and OBS calibrations were performed by the University of Utrecht.

References

Aagaard, T., Greenwood, B., 2008. Infragravity wave contribution to surf zone sediment transport - the role of advection. Mar. Geol. 251, 1–14. https://doi.org/10.1016/j.margeo.2008.01.017.

Aagaard, T., Jensen, S.G., 2013. Sediment concentration and vertical mixing under breaking waves. Mar. Geol. 336, 146–159. https://doi.org/10.1016/j.margeo.2012.11.015.

Aagaard, T., Brinkkemper, J., Christensen, D.F., Hughes, M.G., Ruessink, G., 2021. Surf Zone Turbulence and Suspended Sediment Dynamics— A Review. J. Marin. Sci. Eng. 9, 1300. https://doi.org/10.3390/jmse9111300.

Ahrens, J.P., 2000. A Fall-Velocity Equation. J. Waterw. Port Coast. Ocean Eng. 126, 99–102. https://doi.org/10.1061/(asce)0733-950x(2000)126:2(99).

Arcilla, A., Roelvink, J., O'Connor, B., Reniers, A., Jimenez, J., 1994. The Delta Flume '93 experiment. Coast. Dynam. 488–502.

Bailard, J.A., 1981. An energetics total load sediment transport model for a plane sloping beach (longshore transport). J. Geophys. Res. 86, 10938–10954. https://doi.org/10.1029/JC086iC11p10938.

Battjes, J.A., Janssen, J.P., 1978. Energy loss and set-up due to breaking of random waves. In: Proceedings of the Coastal Engineering Conference, 1. ASCE, pp. 569–587. https://doi.org/10.9753/icce.v16.32.

Butt, T., Russell, P., Puleo, J., Miles, J., Masselink, G., 2004. The influence of bore turbulence on sediment transport in the swash and inner surf zones. Cont. Shelf Res. 24, 757–771. https://doi.org/10.1016/j.csr.2004.02.002.

Campbell Scientific Inc, 2008. Operator's Manual OBS-3+ Suspended Solids and Turbidity Monitor. Technical Report Campbell Scientific Inc.

Castelle, B., Marieu, V., Bujan, S., Splinter, K.D., Robinet, A., Sénéchal, N., Ferreira, S., 2015. Impact of the winter 2013-2014 series of severe Western Europe storms on a double-barred sandy coast: Beach and dune erosion and megacusp embayments. Geomorphology 238, 135–148. https://doi.org/10.1016/j.geomorph.2015.03.006.

Dally, W.R., Dean, R.G., 1984. Suspended Sediment Transport and Beach Profile Evolution. J. Waterw. Port Coast. Ocean Eng. 110, 15–33. https://doi.org/10.1061/(asce)0733-950x(1984)110:1(15).

de Winter, R.C., Gongriep, F., Ruessink, B.G., 2015. Observations and modeling of alongshore variability in dune erosion at Egmond aan Zee, the Netherlands. Coast. Eng. 99, 167–175. https://doi.org/10.1016/j.coastaleng.2015.02.005.

Deigaard, R., 1993. A note on the three-dimensional shear stress distribution in a surf zone. Coast. Eng. 20, 157–171. https://doi.org/10.1016/0378-3839(93)90059-H.

Den Heijer, C., 2013. The Role of Bathymetry, Wave Obliquity and Coastal Curvature in Dune erosion Prediction. Ph.D. thesis. Delft University of Technology. https://doi.org/10.4233/uuid:824df068-8046-414c-a1cc-7d159718918e.

Duncan, J.H., 1981. An Experimental Investigation of breaking Waves Produced by a Towed Hydrofoil. In: Proceedings of the Royal Society of London. Series A, Mathematical and Physical Sciences, 377, pp. 331–348.

Eichentopf, S., van der Zanden, J., Cáceres, I., Baldock, T.E., Alsina, J.M., 2020. Influence of storm sequencing on breaker bar and shoreline evolution in large-scale experiments. Coast. Eng. 157, 103659 https://doi.org/10.1016/j.coastaleng.2020.103659.

Elgar, S., Raubenheimer, B., Guza, R.T., 2001. Current meter performance in the surf zone. J. Atmos. Ocean. Technol. 18, 1735–1746. https://doi.org/10.1175/1520-0426(2001)018<1735:CMPITS>2.0.CO;2.

Elgar, S., Raubenheimer, B., Guza, R.T., 2005. Quality control of acoustic Doppler velocimeter data in the surfzone. Meas. Sci. Technol. 16, 1889–1893. https://doi.org/10.1088/0957-0233/16/10/002.

Feddersen, F., Fincham, A.M., Brodie, K.L., Young, A.P., Spydell, M.S., Grimes, D.J., Pieszka, M., Hanson, K., 2023. Cross-shore wind-induced changes to field-scale overturning wave shape. J. Fluid Mech. 958, 1–28. https://doi.org/10.1017/jfm.2023.40.

Fredsøe, J., 1985. Turbulent boundary layer in wave-current motion. J. Hydraul. Eng. 110, 1103–1120.

Fredsøe, J., Deigaard, R., 1992. Mechanics of Coastal Sediment Transport volume 3 of Advanced Series on Ocean Engineering. World Scientific. https://doi.org/10.1142/1546.

Harley, M.D., Turner, I.L., Splinter, K.D., Phillips, M.S., Simmons, J.A., 2016. Beach response to Australian east coast lows: A comparison between the 2007 and 2015 events, Narrabeen-Collaroy Beach. J. Coast. Res. 1, 388–392. https://doi.org/10.2112/SI75-078.1.

Huynh-thanh, S., Temperville, A., 1990. A numerical model of the rough turbulent boundary layer in combined wave and current interaction. In: Coastal Engineering Proceedings, 22, pp. 853–866. https://doi.org/10.9753/icce.v22.%p.

Leaman, C.K., Harley, M.D., Splinter, K.D., Thran, M.C., Kinsela, M.A., Turner, I.L., 2021. A storm hazard matrix combining coastal flooding and beach erosion. Coast. Eng. 170, 104001 https://doi.org/10.1016/j.coastaleng.2021.104001.

Longuet-Higgins, M.S., 1970. Longshore currents generated by obliquely incident sea waves- 1, 2. J. Geophys. Res. 75, 6778–6801. https://doi.org/10.1029/jc075i033p06790.

Madsen, O.S., 1975. Stability of a sand bed under breaking waves. In: Coastal Engineering Proceedings, 14. ASCE, pp. 776–794. https://doi.org/10.9753/icce.v14.45.

Masselink, G., Puleo, J.A., 2006. Swash-zone morphodynamics. Cont. Shelf Res. 26, 661–680. https://doi.org/10.1016/j.csr.2006.01.015.

Masselink, G., Scott, T., Poate, T., Russell, P., Davidson, M., Conley, D., 2016. The extreme 2013/2014 winter storms: Hydrodynamic forcing and coastal response along the southwest coast of England. Earth Surf. Process. Landf. 41, 378–391. https://doi.org/10.1002/esp.3836.

Myrhaug, D., Slaattelid, O.H., 1990. A rational approach to wave-current friction coefficients for rough, smooth and transitional turbulent flow. Coast. Eng. 14, 265–293. https://doi.org/10.1016/0378-3839(90)90027-T.

Nielsen, P., 1992. Coastal Bottom Boundary Layers and Sediment Transport, 4th ed. World scientific.

Nortek, 2018. Vector (ADV) Manual (Technical Report Nortek).

Ocean Sensor Systems, 2023. OSSI-010-003 Wave Gauge User Manual. Technical Report. Ocean Sensor Systems.

Ogston, A.S., Sternberg, R.W., 2002. Effect of wave breaking on sediment eddy diffusivity, suspended-sediment and longshore sediment flux profiles in the surf zone. Cont. Shelf Res. 22, 633–655. https://doi.org/10.1016/S0278-4343(01)00033-4.

Palmsten, M.L., Holman, R.A., 2011. Infiltration and instability in dune erosion. J. Geophys. Res. Oceans 116, C10030. https://doi.org/10.1029/2011JC007083.

Palmsten, M.L., Holman, R.A., 2012. Laboratory investigation of dune erosion using stereo video. Coast. Eng. 60, 123–135. https://doi.org/10.1016/j.coastaleng.2011.09.003.

RBR Global, 2022. RBR solo and RBR duet Instrument Guide. In: Technical Report RBR Global.

Reniers, A.J., Roelvink, J.A., Thornton, E.B., 2004a. Morphodynamic modeling of an embayed beach under wave group forcing. J. Geophys. Res. Oceans 109. https://doi.org/10.1029/2002jc001586.

Reniers, A.J., Thornton, E.B., Stanton, T.P., Roelvink, J.A., 2004b. Vertical flow structure during Sandy Duck: Observations and modeling. Coast. Eng. 51, 237–260. https://doi.org/10.1016/j.coastaleng.2004.02.001.

Reniers, A.J., Gallagher, E.L., MacMahan, J.H., Brown, J.A., Van Rooijen, A.A., Van Thiel De Vries, J.S., Van Prooijen, B.C., 2013. Observations and modeling of steep-beach grain-size variability. J. Geophys. Res. Oceans 118, 577–591. https://doi.org/10.1029/2012JC008073.

Roelvink, J.A., Stive, M.F., 1989. Bar-generating cross-shore flow mechanisms on a beach. J. Geophys. Res. 94, 4785–4800. https://doi.org/10.1029/JC094iC04p04785.

Roelvink, D., Reniers, A., van Dongeren, A., van Thiel de Vries, J., McCall, R., Lescinski, J., 2009. Modelling storm impacts on beaches, dunes and barrier islands. Coast. Eng. 56, 1133–1152. https://doi.org/10.1016/j.coastaleng.2009.08.006.

Ruessink, B.G., Miles, J.R., Feddersen, F., Guza, R.T., Elgar, S., 2001. Modeling the alongshore current on barred beaches. J. Geophys. Res. Oceans 106, 22451–22463. https://doi.org/10.1029/2000JC000766.

Rutten, J., Tissier, M., van Wiechen, P., Zhang, X., de Vries, S., Reniers, A., Mol, J.-W., 2024. Continuous Wave Measurements Collected in Intermediate Depth throughout the North Sea storm season during the RealDune/REFLEX experiments. Data 9, 70. https://doi.org/10.3390/data9050070.

Sato, S., Homma, K., Shibayama, T., 1990. Laboratory Study on Sand Suspension due to breaking Waves. Coast. Eng. Japan 33, 219–231. https://doi.org/10.1080/05785634.1990.11924534.

Schweiger, C., Kaehler, C., Koldrack, N., Schuettrumpf, H., 2020. Spatial and temporal evaluation of storm-induced erosion modelling based on a two-dimensional field case including an artificial unvegetated research dune. Coast. Eng. 161 https://doi.org/10.1016/j.coastaleng.2020.103752.

Shemdin, O., Hasselmann, K., Hsiao, S.V., Herterich, K., 1978. Nonlinear and Linear Bottom Interaction Effects in Shallow Water. In: Favre, A., Hasselmann, K. (Eds.), Turbulent Fluxes through the Sea Surface, Wave Dynamics, and Prediction. Springer US, Boston, MA, pp. 347–372. https://doi.org/10.1007/978-1-4612-9806-9 {_}23. URL:

Smith, G.G., Mocke, G.P., 2002. Interaction between breaking/broken waves and infragravity-scale phenomena to control sediment suspension transport in the surf zone. Mar. Geol. 187, 329–345. https://doi.org/10.1016/S0025-3227(02)00385-7.

Soulsby, R.L., 1998. Dynamics of Marine Sands. Thomas Telford Ltd. https://doi.org/10.1680/doms.25844

Soulsby, R.L., Hamm, L., Klopman, G., Myrhaug, D., Simons, R.R., Thomas, G.P., 1993. Wave-current interaction within and outside the bottom boundary layer. Coast. Eng. 21, 41–69. https://doi.org/10.1016/0378-3839(93)90045-A.

Steetzel, H.J., 1993. Cross-Shore Transport during Storm Surges. Ph.D. thesis. Delft University of Technology. https://doi.org/10.1061/9780872627765.147.

Stive, M., De Vriend, H., 1987. Quasi-3D Nearshore Current Modelling: Wave-Induced secondary current. In: Conference on Coastal Hydrodynamics. American Society of Civil Engineers, New York, pp. 356–370.

Swart, D., 1974. Offshore Sediment Transport and Equilibrium Beach Profiles. Ph.D. thesis. Delft University of Technology. URL: https://repository.tudelft.nl/islandora/object/uuid:057cb136-5f5b-484a-878d-5616fbaeda4e.

Thornton, E.B., Guza, R.T., 1983. Transformation of wave height distribution. J. Geophys. Res. Oceans 88, 5925–5938. https://doi.org/10.1029/JC088iC10p05925.

van Bemmelen, C.W., de Schipper, M.A., Darnall, J., Aarninkhof, S.G., 2020. Beach scarp dynamics at nourished beaches. Coast. Eng. 160, 103725 https://doi.org/10.1016/j.coastaleng.2020.103725.

van der A, D.A., Ribberink, J.S., Van der Werf, J.J., O'Donoghue, T., Buijsrogge, R.H., Kranenburg, W.M., 2013. Practical sand transport formula for non-breaking waves and currents. Coast. Eng. 76, 26–42. https://doi.org/10.1016/j.coastaleng.2013.01.007. URL.

van der Zanden, J., Van Der, A.D.A., Hurther, D., Cáceres, I., O'Donoghue, T., Ribberink, J.S., 2017. Suspended sediment transport around a large-scale laboratory breaker bar. Coast. Eng. 125, 51–69. https://doi.org/10.1016/j.coastaleng.2017.03.007.

van Gent, M.R., van Thiel de Vries, J.S., Coeveld, E.M., de Vroeg, J.H., van de Graaff, J., 2008. Large-scale dune erosion tests to study the influence of wave periods. Coast. Eng. 55, 1041–1051. https://doi.org/10.1016/j.coastaleng.2008.04.003.

van Rijn, L.C., 1984. Sediment Transport, Part II: Suspended load Transport. J. Hydraul. Eng. 110, 1613–1641. https://doi.org/10.1061/(asce)0733-9429(1984)110:11(1613).

van Rijn, L.C., 1993. Principles of Sediment Transport in Rivers. Estuaries and Coastal Seas.

van Rijn, L.C., Havinga, F.J., 1995. Transport of Fine Sands by Currents and Waves. II. J. Waterw. Port Coast. Ocean Eng. 121, 123–133. https://doi.org/10.1061/(asce)0733-950x(1995)121:2(123).

van Rijn, L.C., Kroon, A., 1993. Sediment transport by currents and waves. Proc. Coast. Eng. Conf. 3, 2613–2628. https://doi.org/10.1061/9780872629332.199.

van Thiel de Vries, J.S.M., Clarke, L.B., Aarninkhof, S.G., Coeveld, E.M., Holman, R.A., Palmsten, M.L., Reniers, A.J., Stive, M.J., Uijttewaal, W.S., 2007. Interaction of dune face and swash zone. In: Coastal Sediments '07 - Proceedings of 6th International Symposium on Coastal Engineering and Science of Coastal Sediment Processes. American Society of Civil Engineers, Reston, VA, pp. 1975–1987. https://doi.org/10.1061/40926(239)155.

van Thiel de Vries, J.S.M., van Gent, M.R., Walstra, D.J., Reniers, A.J., 2008. Analysis of dune erosion processes in large-scale flume experiments. Coast. Eng. 55, 1028–1040. https://doi.org/10.1016/j.coastaleng.2008.04.004.

van Wiechen, P., Rutten, J., de Vries, S., Tissier, M., Mieras, R., Anarde, K., Baker, C., Reniers, A., Mol, J.-W.. Nearshore Coastal Measurements of Calm, Moderate, and Storm Conditions at Two Artificial Dunes along the Dutch Coast during the RealDune/REFLEX Experiments. URL. https://data.4tu.nl/collections/0a05d041-00b6-4e8e-a5c5-70e624ea720b.

van Wiechen, P., de Vries, S., Reniers, A., Aarninkhof, S., 2023b. Dune erosion during storm surges: A review of the observations, physics and modelling of the collision regime. Coast. Eng. 186, 104383 https://doi.org/10.1016/j.coastaleng.2023.104383.

van Wiechen, P., Rutten, J., de Vries, S., Tissier, M., Mieras, R., Anarde, K., Baker, C., Reniers, A., Mol, J.-W., 2024. Measurements of dune erosion processes during the RealDune/REFLEX experiments. Sci. Data 11, 421. https://doi.org/10.1038/s41597-024-03156-9.

Yang, S., Yang, W., Zhang, C., Qin, S., Wei, K., Zhang, J., 2022. Experimental and numerical study on the evolution of wave front profile of dam-break waves. Ocean Eng. 247, 110681. URL. https://doi.org/10.1016/j.oceaneng.2022.110681.